An adsorption-precipitation model for the formation of injector external deposits in internal combustion engines

Radomir I. Slavchov*[,1], Sebastian Mosbach[1], Markus Kraft[1,2], Richard Pearson[3], Sorin V. Filip[3]

[1]Department of Chemical Engineering and Biotechnology
University of Cambridge
West Site, Philippa Fawcett Drive
Cambridge, CB3 0AS
United Kingdom
*E-mail: ris26@cam.ac.uk

[2] School of Chemical and Biomedical Engineering
Nanyang Technological University
62 Nanyang Drive
Singapore, 637459

[3]BP International Ltd,
Technology Centre
Whitchurch Hill
Pangbourne
Berkshire, RG8 7QR
United Kingdom

Abstract

The occurrence of deposits on fuel injectors used in gasoline direct injection engines can lead to fuel preparation and combustion events which lie outside of the intended engine design envelope. The fundamental mechanism for deposit formation is not well understood. The present work describes the development of a computational model and its application to a direct injection gasoline engine in order to describe the formation of injector deposits and quantify their effect on injector operation. The formation of fuel-derived deposits at the injector tip and inside the nozzle channel is investigated. After the end of an injection event, a fuel drop may leak out of the nozzle and wet the injector tip. The model postulates that the combination of high temperature and the presence of NO_x produced by the combustion leads to the initiation of a reaction between the leaked fuel and the oxygen dissolved in it. Subsequently, the oxidation products attach at the injector surface as a polar proto-deposit phase. The rate of deposit formation is predicted for two limiting mechanisms: adsorption and precipitation. The effects of the thermal conditions within the engine and of the fuel composition are investigated. Branched alkanes show worse deposit formation tendency than n-alkanes. The model was also used to predict the impact of injector nozzle deposit thickness on the rate of fuel delivery and on the temperature of the injector surface.

Keywords: injector deposits, deposition rate model, liquid fuel oxidation, DISI engine, injector tip temperature, NO_x

1 Introduction

Modern engines use injectors that must insert a fuel jet of very high velocity into the hot gases in the cylinder with good precision in terms of amount of fuel added, timing of the injection event and the spray shape. The accurate timing of the injection in gasoline and some diesel engines depends on the efficient sealing of the fuel pathway, realized by the injector needle seating onto the entrance of the nozzle channels. This seal is never perfect, and under the action of the high injection pressure (Δp ~ 10-40 MPa for gasoline; cf. the S6 supplement for a list of symbols), fuel droplets leak out of the nozzle after the end of the intended injection event, wetting the nozzle channel and the injector tip surfaces [1-3]. The leakage appears in at least two stages:

(i) The non-steady end-of-injection fuel dribble immediately after injection, due to needle bouncing and capillary forces acting on the jet when it breaks off the nozzle. In this case, a significant amount of fuel may remain attached at the injector tip, wetting the surface [2,4].

(ii) A slower steady leakage (*static fuel dribble*) [3] due to Poiseuille flow through the imperfect seal acts during the whole engine cycle, and leads to accumulation of fuel at the injector surface when the cylinder pressure is high enough [1] to prevent vaporization of the fuel.

The leaked fuel remains exposed to heat and combustion gases for certain period, and, before evaporating completely, the liquid degrades. The degradation products remain at the injector surface, eventually developing into carbonaceous deposits.

Injector deposits have existed since the invention of the fuel injector, but they became a significant problem only with the recent advances in the injector technology, both in diesel [5,6] and gasoline [7-9] engines. The combined requirements for high precision and small nozzle radii (R_n ~ 50 μm) mean that a very small amount of *nozzle channel deposits* can result in a serious dysfunction of the injector. For example, even a deposit layer as thin as 1 μm can cause a reduction in geometric flow area of 4%. The *nozzle tip deposits* cause distortion of the optimum spray pattern [5,8,10,11], may heat up to high temperatures, and tend to soak with fuel due to their porosity [3,12]. The *needle ball and seat deposits* [8] can spoil the seal, leading to increased leakage rate.

The studies of the injector deposits meet with serious difficulties. The first obstacle is that the *deposition process is very slow*. The accumulation of an observable amount of deposit requires many hours of engine operation [1]. For this reason, many studies and standardized tests of fuels and machinery are accelerated in some way, e.g.: the fuel is artificially additized with a fouling agent that produces deposits [13-15]; fuel formulations with high levels of olefins and sulfur are often utilized (like the "plugging" fuel of Bacho et al. [16]); sometimes the degradation is investigated at increased partial pressure of O_2 [17]. The second obstacle is that, once formed, the *deposits experience complicated evolution* [18]. This causes uncertainty in the literature regarding their composition – the deposit that is initially formed has little to do with the deposit one finds after 30 hours of engine operation with concomitant exposure to high temperature, combustion gases, lubricant mist, and corrosion products. A third obstacle is that the field deposits are often caused by problems specific to a particular fuel or engine.

Given the above, it is likely that there is no single general mechanism of formation of injector deposits. Yet, there are several general features of the deposit formation that seem to be valid not only at the injector surface but anywhere in the engine:

(i) the engine deposits are formed in a *liquid hydrocarbon* phase, and the existence of fuel (or lubricant) in the liquid state is a requirement for them to occur [1,19-22].

(ii) The deposits are a polydisperse mixture of polar oxidized hydrocarbons (HCs) with dispersed organic and inorganic salts [5,8,23-25].

(iii) The deposit growth process occurs at a hydrophilic surface in contact with a hydrophobic fluid. For the injector, this is the interface of *polar deposit*|*liquid fuel*. With brand new injectors, it could be the metal oxide|liquid fuel or the metal oxide|lubricant interface instead.

Generally, every component of the injector that is in contact with hot liquid fuel inevitably experiences deposit formation. Fuel degradation is observed in the common rail supplying the individual injectors and its filters [26]. The *internal injector deposits* found on the needle and the pressure control valve [27] are a serious problem in diesel engines. They are similar in nature to the soapy deposits found on the fuel filter – we do not consider this type of fouling in the present work. Instead we are mainly interested in the *external injector deposits* [5-8], which are common with direct injection spark ignition (DISI) gasoline engines, where they accumulate at the injector tip, inside the nozzle channel[1] and even deeper inside the nozzle, on the needle ball and its seating area [8,28]. Diesel fuels normally would not cause deposits inside the nozzle channel [5]. Most of the deposited material at the injector tip is fuel-derived, bearing chemical similarities with fuel gum [28], but blended with lubricant elements with a concentration of the latter increasing with distance from the nozzle hole [8,17]. The chemistry of the fuel affects the injector deposits very significantly, especially when polar blends are used. Thus, for gasoline, an ethanol blend results in lower deposit propensity [8,29]; conversely, the relatively polar biodiesel components found in market diesel blends lead to more deposits. Unlike mineral diesel, biodiesel forms deposits inside the nozzle channels of the injector [5].

The initial nascent deposit, or proto-deposit, could be a viscous liquid (e.g., [18]) containing products of the low-temperature oxidative degradation of the fuel (such as alkylhydroperoxides, aldehydes, ketones, alcohols, ethers and acids, found in the tip deposits – e.g., [6]). Certain aromatic species native to the fuel are also found in the deposit [6,30]. As the deposit evolves and ages, it loses the organic oxygen – for example, the fresh deposit at the diesel injector tip contains 20 *w*% oxygen [5], while the aged carbonaceous material located further away from the nozzle is of decreased oxygen content (~10 *w*%). The deposit evolution leads also to increased aromatic content, porosity, and advanced polymerization. Lubricant- and corrosion-derived material stick to the deposit, eventually forming together with the organics the familiar reinforced composite material that can be so hard to remove.

The precursors of the external gasoline injector deposits, according to Ref. [8], are polar compounds present in the fuel, peroxides, and ash (resulting from combustion of the lubricant). It has been claimed that two main chemical routes contribute to the formation and the evolution of the injector deposits – low-temperature autoxidation [8,17,31] and high-temperature pyrolysis [8,17], with subsequent isomerization and polymerization of the fuel [17]. Indeed, there is a strong correlation between the outcome of various standardized liquid phase oxidation bench tests and rate of deposit formation [24]. Indicators in use that exploit this correlation include: the induction time for the onset of the intensive consumption of oxygen for gasoline in a closed reactor at 100°C and 1 atm O_2; the mass of the oxidation products formed at 110°C over a 6 h period in air [24]; the peroxide number [16]. On the other hand, the formation of polyaromatic hydrocarbons occurs at around 350°C [8] and is probably a secondary process. The metallic substrate may influence these processes by acting as a catalyst [8]. A separate process that contributes to the injector fouling is the deposition of lubricant-derived salts (ash), which we will not consider here.

[1] There is confusion in the literature over the terminology used for nozzle channel deposits: many researchers call both the orifice and the tip deposits "external injector deposits"; others prefer to use "external" for tip deposits only, as opposed to the "internal" channel deposits. We utilize the former terminology, as it offers a better contrast to the internal deposits on the needle and control valve found in diesel injectors. More specifically, in this work, "external" indicates possiblility for contact with combustion gases, and "internal" means that there is no such possibility.

Venkataraman and Eser [6] reported interesting data on the microstructure of the *injector tip deposits*. The material contains clusters of spherical particles forming densely packed aggregates, with large voids between the aggregates. The clusters appear to have uniform size distribution. This suggests the deposit phase grows *in the bulk* of the liquid phase, with subsequent precipitation. The vaporization of the fuel is the process that induces the precipitation. This agrees (at least broadly) with the mechanism of Kinoshita et al. [7] for the formation of gasoline injector deposits. *Nozzle channel deposits*, on the other hand, appear more compact – probably, upon each injection event, the turbulent flow mechanically removes the loosely attached particles stemming from the bulk phase and only truly interfacial processes contribute to the rate of formation.

While there are studies of the fuel degradation mechanism under steady laboratory test conditions (e.g. [32,33]; reviewed in [1]), to our knowledge, only one study [1] attempts to model the degradation under (diesel) engine operating conditions. There are several major differences between conditions existing within an operating engine and these found in rigs under laboratory test conditions – these are summarized in **Table 1** and explained in more detail in the following sections. Engine operating conditions complicate significantly the experimental investigation of injector deposits, leading to incomprehensible and sometimes contradictory results in the literature. Xu et al. [8] summarize the situation as follows: *"…The mechanism of GDI injector deposit formation is not completely understood. The only proposed mechanism available in the literature concerns the deposit precursors, the $T_{90\%}$ parameter of the fuel, and injector nozzle temperature. There is a lack of agreement of the role of nozzle temperature and $T_{90\%}$ in GDI injector formation…"* A lot of information about the deposition can be gained on theoretical grounds. The general mechanism of fuel degradation is known in detail [34,35], and one can predict the fate of the fuel droplet exposed to the cylinder gases in a semi-quantitative manner. In the present work the application of modelling is intended to provide better comprehension of the role of the distillation characteristics of the fuel and the injector surface temperature, as sought by Xu et al. [8]. The conditions at the injector tip (variations of pressure, temperature, gas phase composition) are more readily modelled than measured experimentally. Modelling can be used also to understand some of the basic effects that deposits have on injector operation – the effect of the nozzle channel deposits on the injection flow rate [5,8,17] and the effect of the injector tip deposits on the tip temperature are particularly interesting and are dealt with below.

Table 1: Comparison of peculiarities of fuel degradation under laboratory rig conditions and within an engine cylinder under fired operating conditions.

Laboratory rig conditions [1,32,33]	**In-cylinder conditions in an operating engine**
initiation by O_2, or forced initiation by R_2O_2	initiation by NO_2, branching by NO
steady process: temperature T and initiation rate v_i are constant or change slowly; quasi-steady regime for $RO_2\cdot$	*cyclic process*: fast variations of T, fast variations of v_i; cyclic accumulation of $RO_2\cdot$
continuous degradation; significant time for reaction and conversion level	cyclic; milliseconds for reaction, small conversion for one cycle

Our aim in this study is to make an attempt to rationalize the existing observations for the deposit formation process, by simulating the degradation of model fuels under engine operating conditions. Simulation of an engine operating cycle is performed to define all relevant

physicochemical conditions in the required detail. We also investigate the effect the injector deposits have on the thermal conditions at the surface of the injector and the injected amount of fuel. The predictions of the model are compared with qualitative and quantitative experimental data available in the literature. Order-of-magnitude estimates allow us to discard some of the seemingly possible hypotheses for the mechanism of deposition and to formulate a model that does not contradict the observations.

2 Mechanisms of deposit formation

In accordance with the brief review above, we assume that the deposit formation is the result of the following sequence of events.

(i) After the injection, a fuel droplet leaks out of the injector [1,2]. At the peak of the cylinder pressure, this droplet is below its boiling temperature and its temperature is close to that of the surface of the injector tip, T_{tip}.

(ii) During the combustion event, the cylinder heats up, the droplet is bombarded by radicals produced by the combustion process, and degrades.

(iii) As pressure decreases late in the power stroke, the droplet starts to boil. The non-volatile degradation products either precipitate in the fuel film (as hypothesized in Ref. [7]) or adsorb at the surface.

The observations in Ref. [6] suggest that the tip deposit is made of the precipitated material. On the other hand, whatever material precipitates in the nozzle channel will be washed away with the next injection, and only the material which is strongly adsorbed directly at the surface can withstand the turbulent shear of the fuel flow within the nozzle. These two modes of accumulation can be considered as two limiting cases: the precipitation mechanism gives the largest possible rate of deposit formation; the adsorption mechanism gives the smallest one.

2.1 Conditions in the fuel film and the quench layer

2.1.1 Engine model

A virtual model of a real DISI test engine is constructed using the *SRM Engine Suite* software [36]. The simulation uses the *stochastic reactor model* (SRM) – a zero-dimensional model based on a discretization of the probability density function transport models [37]. It splits the cylinder charge into an ensemble of *stochastic particles* that represents the distribution of the composition, temperature etc. within the cylinder. This method is very suitable for problems involving complicated chemical processes occurring in a turbulent environment. The implemented mechanism of the combustion process in the gas phase involves 208 species and 1002 reactions (provided in Ref. [38]). The turbulent mixing process is modelled with the *Euclidean minimum spanning tree* technique [39]. The software contains also sub-models of a number of relevant processes in the engine, including the stochastic heat transfer [40], the piston movement, the spark ignition event [41], and the direct injection of fuel [42]. It has been validated against data for a variety of gasoline and diesel, spark- and compression-ignition engines, with fuels of different composition, cf. e.g. Refs. [40-44].

The parameters describing the engine are listed in **Table 2** (a more detailed description is given in S1). The engine operates with stoichiometric mixture. Full-load conditions were modelled at 2840 rev/min, resulting in an air supply of 23.8 kg/h per cylinder. Early injection strategy is applied: in the real engine, the injection starts at -311 crank angle degrees (CAD) with respect to the top dead centre (TDC) of the power stroke (49° after TDC of the gas

exchange stroke) – i.e. the fuel is injected while air intake valve is still open. Atomization and mixing are assumed to be already complete when the inlet valve closes shortly after bottom dead centre (BDC). Only the range from -180 to 180 CAD is simulated.

The engine model was used to calculate representative thermal boundary conditions for the later deposit formation study. The exhaust gas is not recirculated in the real engine we model, yet residual exhaust is present in the initial charge and is essential for the correct calculation of the relevant engine experimental parameters (the pressure profile, in particular). 6% of the oxygen element present in the cylinder after the inlet valve closes is in the form of trapped CO_2, H_2O, CO and NO left from the previous cycle (the assumed initial composition is given in S1). Another major effect of the presence of the hot exhaust in the cylinder is the elevated initial temperature (82°C) of the charge at inlet valve closure and the consequent reduced mass of air.

Table 2: Model DISI engine parameters (for 1 cylinder).

Parameter	**Value**		
Displaced volume	400 cm^3		
Bore	79 mm		
Stroke	81.4 mm		
Compression ratio	10:1		
Speed, ν	2840 rev/min		
Air flow rate	23.8 kg/h		
Fuel flow rate	1.6 kg/h		
Equivalence ratio	1		
Spark timing	-19 CAD		
	simulation	**experiment**	**difference**
Fuel	PRF95	E10	
IMEP	0.775 MPa	0.67 MPa	16%
MFB50	14 CAD	10 CAD	4 CAD
Maximum cylinder pressure	3.7 MPa	3.7 MPa	< 1%

The test engine data have been measured under the specified conditions but with E10 gasoline (10% ethanol blend in a mixture of hydrocarbons); the model fuel in the virtual engine is PRF95 (95 *w*% isooctane, 5 *w*% n-heptane). The two fuels have similar lower heating value and octane number, therefore, similar pressure and temperature profile can be expected. Indeed, the virtual engine represents well the maximum pressure (less than 1% error) and the MFB50 timing of the test engine (the point at which 50% of the fuel mass is burned; 4 CAD difference, cf. Table 2). The indicated mean effective pressure (IMEP) is also reasonable, in view of the fuel difference and the approximated calculation of the exhaust & intake strokes contribution (IMEP prediction error 16%).

2.1.2 Leakage of fuel and temperature of the fuel film

Discharge of fuel after the intended injection event is an undesirable phenomenon, as it results in uncontrolled addition of fuel to the cylinder in a poorly prepared state. The rate of leakage of fuel out of the nozzle of a diesel injector has been shown to vary during a cycle [2] and this is likely to be the case for gasoline injectors, even though they operate at lower injection pressures. The authors are not aware of data in the literature quantifying the variation of fuel dribble rate with time (cf. Ref. [1] for an attempt to model it). Another complication is that the unsteady end-of-injection leakage can be expected to produce droplets of different volume on each cycle, in relation to the chaotic nature of the spray evolution close to the point of jet breakage [45]. For clean injectors, the typical value of the leaked amount is 0.1% of the injected

fuel mass [46]; the target maximum static leakage through the seat of a brand new DISI engine injector is typically 1.5 mm^3/min at Δp = 10 MPa [3]. Leakage causes deposits, but the opposite may also be the case: it was found that deposits can cause severe leakage [9], probably due to their occurrence on the ball at the end of the needle and on its seat [8].

An important feature of the leakage in the engine is that the conditions are usually such that the fuel is below its boiling temperature T_b when the piston is near the TDC and the pressure is high, but then, as pressure falls later in the combustion stroke, the leaked droplet reaches its boiling point. If this is the case, we will speak about *deposition in the boiling regime*. The boiling was observed experimentally in an injector test rig in Ref. [47]. Hexadecane was injected in the rig; after the end of the injection, a fuel droplet leaked out of the nozzle exit while the conditions were still near the peak pressure (~5 MPa). The droplet grew until it started to boil visibly at about +50 CAD. A few CA degrees later, the droplet had vaporized completely, leaving behind a black residue [47]. This residue can be assumed to be the proto-deposit phase from which the deposits arise.

The point of boiling is thus of obvious importance for the deposition process. In this initial work, to determine it, we assume that the fuel behaves as a single-component liquid (which is reasonable for PRF95), and its boiling temperature T_b is related to the cylinder pressure p through the Clausius-Clapeyron equation:

$$T_b = T_{b0}\left(1 - \frac{RT_{b0}}{\lambda_b}\ln\frac{p}{p_0}\right)^{-1}. \qquad (1)$$

Here T_{b0} is the boiling temperature of the fuel at standard pressure (p_0 = 101325 Pa) – for PRF95, $T_{b0} \approx 373$ K [48]. R is the universal gas constant; λ_b is the heat of vaporization ≈ 31 kJ/mol for PRF95 (estimated as the vaporization heat of isooctane using *eq. 18* in Ref. [49]. The vapour pressure predicted by Eq (1) differs by no more than 6% from that of isooctane in the interval 80-220°C. The simulated cylinder pressure profile in the SRM engine and the respective change of the boiling temperature with time are shown in **Figure 1**.

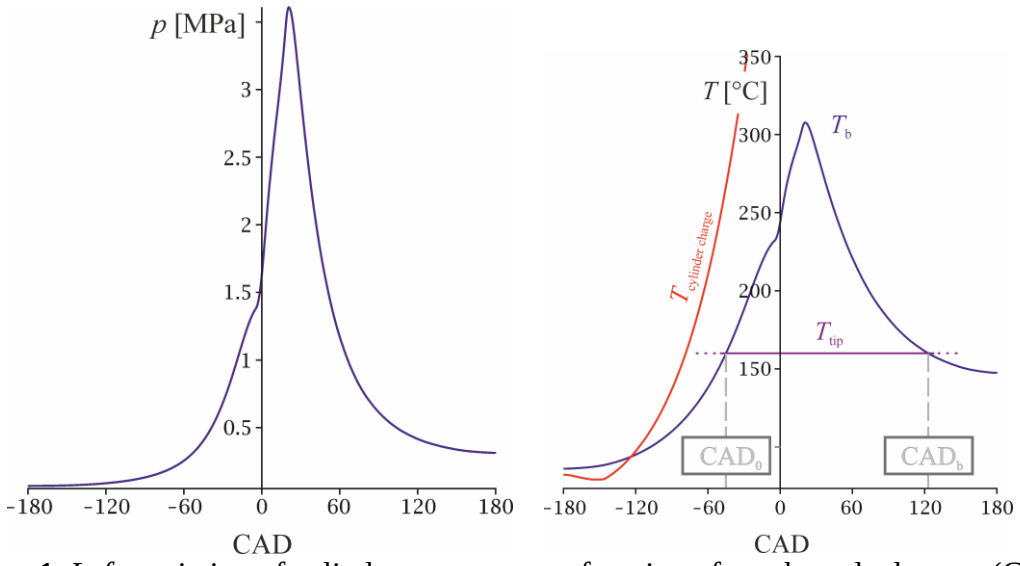

Figure 1. *Left*: variation of cylinder pressure p as function of crank angle degrees (CAD) during the engine cycle (SRM Engine Suite simulation). *Right*: variation of boiling temperature T_b (blue line, calculated via Eq (1)), simulated temperature of the combustion gases ($T_{\text{cylinder charge}}$ – red line), and average injector tip surface temperature (T_{tip} – purple line, set to 160°C) during the engine cycle. Between CAD_0 and CAD_b (where $T_b > T_{tip}$), leaking fuel accumulates. This fuel vaporizes completely when the boiling point drops below T_{tip} (outside the range CAD_0 to CAD_b).

A typical gasoline injector surface temperature (T_{tip}) is in the range 120-190°C [50], therefore, during each cycle, the boiling temperature of the leaked droplet changes from well below the average surface temperature to well above it. This suggests the following evolution of the injector dribble:

(i) early in the compression stroke, where $T_b < T_{tip}$, the fuel film will be boiling, and its temperature will remain equal to T_b as long as liquid phase is present. No or little accumulation of liquid fuel is possible. This means that the fuel due to the unsteady leakage (immediately after the injection) is relatively unimportant for the deposition process for the engine studied. Due to the early injection strategy, the end-of-injection leakage will boil off fast, unless its amount is large enough for its vaporization to cool down the injector significantly.

(ii) As the pressure increases, so does T_b, until the point where $T_b = T_{tip}$ is reached (*start of the accumulation* – CAD_0 in Figure 1). At CAD_0, boiling ceases; the fuel film temperature will remain equal to T_{tip}. This situation will continue after the pressure peak, until p decreases to the point where T_b drops below T_{tip} again.

(iii) At this point, the fuel will swiftly vaporize and the non-volatile residue will precipitate at the injector surface (*point of boiling and precipitation* – CAD_b in Figure 1).

Thus, during the whole process, the temperature of the fuel film around the injector nozzle, if such a film is present, will be approximately equal to the smaller of T_b and T_{tip}, i.e.

$$T^F = \min(T_b, T_{tip}), \tag{2}$$

where T^F is the temperature controlling the rate of fuel degradation, and, respectively, the rate of deposit formation. Thus, both wall temperature and boiling characteristics are important for the deposition, in agreement with the experimental findings [7,8,17].

The deposit model described in the present work mainly concerns the initial stage of the fuel degradation process (the one that occurs in the liquid phase). It will be assumed below that this stage starts at CAD_0 and ends at CAD_b – i.e. the degradation takes place while leaked fuel accumulates at the injector tip. The points CAD_0 and CAD_b are controlled by the fuel boiling point T_b. During the fuel film accumulation, $T^F = T_{tip}$. For a multicomponent fuel, instead of a single boiling point CAD_b, a *range* of boiling will occur (e.g. [22], *sec.4.5.4* of Ref. [51]), which will contribute to the degradation process significantly – this additional level of complexity will be analysed in future work.

Within the SRM engine model, the injector surface temperature is an independent variable, unrelated to the cylinder pressure profile and therefore, unrelated to the T_b vs. CAD characteristic. Consequently, the dependence of CAD_0 and CAD_b on the injector wall temperature follows directly from **Figure 1** (the blue line in **Figure 1**-*right* is a plot of the inverse function T_{tip}(CAD), as illustrated in Figure S1 in S1). In the normal range of gasoline injector surface temperatures and the considered fuel, CAD_0 ranges between -72 and -20° and the point of boiling, CAD_b, is larger than +69°. At low tip temperatures (below 149°C for the case in Figure 1), or for fuels of low volatility, conditions are possible where the leaked fuel never boils – in this case, instead of the boiling regime, a qualitatively different and supposedly slower regime of deposit formation can be expected to occur (*cold injector regime*, cf. Figure S1). In the other limit – where the injector surface is very hot (T_{tip} > 308°C for the case in Figure 1) or fuel is volatile – the fuel will boil throughout the cycle without accumulation, and thus it will not stay exposed for significant periods to the action of radicals produced by the combustion gases. This case would correspond to a third, *hot injector* regime of deposition (Figure S1). Once the droplet approaches the hot injector regime, the deposit formation rate should decrease again – indeed, at high injector temperatures, less deposition is sometimes observed [50]. These two regimes will not be considered here.

A complicated question that is relevant to the rate of deposition occurs: what is the volume of the leaked droplet? Even if the leakage rate is constant, which is hardly the case [2,46,1], the droplet size will be increasing during the high pressure period between CAD_0 and CAD_b

(although the evaporation rate may be a limiting factor, cf. Eq (52) in S3). After CAD_b, as the fuel boils, the volume is expected to decrease swiftly to zero. In the absence of data, we assume that the volume of the droplet is constant between CAD_0 and CAD_b (while $T_{tip} < T_b$), and is negligibly small otherwise. The respective average thickness of the fuel film (or droplet height) is assumed to be ~100 μm while $T_{tip} < T_b$, as follows from direct observations [47], i.e.

$$h^F/[\mu m] = 100 \times \eta(CAD - CAD_0) \times \eta(CAD_b - CAD), \quad (3)$$

where η is the Heaviside step function.

2.1.3 Modelling the quench layer

The fuel film at the injector tip exchanges matter with the cylinder charge through the cold quench layer in direct contact with the film. The transport of combustion products from the bulk gas to the quench layer is a complicated phenomenon involving numerous unknown characteristics of the turbulent transport. The boundary conditions are also unclear, due to many possible surface reactions. The composition of this layer is of paramount importance for the degradation process. Due to the low temperature and the high oxygen concentration in the quench layer, the reactivity and the concentrations of radicals there change drastically compared to the cylinder bulk. Therefore, even in case of efficient mixing, the mean composition of the cylinder will be very different from the one next to the injector wall.

To model the quench layer, we use a modification of the zone functionality of the SRM Engine Suite [42]. The cylinder charge is separated into two zones: a main zone (*cylinder bulk*) and an auxiliary wall zone (*injector quench layer*). In our modification, the mass of the quench layer zone is set to a negligibly small fraction of that of the cylinder charge (1/50000 – the exact value does not affect the results). The temperature of the quench layer zone is fixed to T_{tip} of the injector surface. The two zones are allowed to exchange mass as described in Ref. [42]. The species transported from the combustion gases to the cold quench layer react in the auxiliary zone, following the implemented reactions [38].

This rough quench layer model has a single transport parameter: the pair mixing fraction ξ [42], controlling the mass exchange between the two zones. This parameter is proportional to the turbulent transport intensity. It is an empirical constant of unknown "best" value; we were able to bound its value within three orders of magnitude (10^{-6}–10^{-4}) outside which the quench layer composition is unreasonable (if $\xi \to 0$, the composition of the quench layer is almost equal to the one of the initial charge; if $\xi \to \infty$, the composition of the quench layer becomes equivalent to that in the cylinder). When $\xi = 5\times10^{-5}$ the order of magnitude of the final deposition rates in a few test cases was reasonable compared to the experimental values. We further used this value for all simulations. We estimated that this value of ξ corresponds to a characteristic time of mixing during the power stroke of the quench layer and the cylinder charge of the order of 100 ms, cf. S1. In the absence of experimental data, the value of ξ has not been further adjusted. It is also implicitly assumed in our model that during intake and exhaust strokes, the mixing is much more efficient (due to the lower gas density and the intensive gas convection) so that most of the quench layer content is exchanged with fresh charge before the inlet valve closes.

In the mechanism we consider below, the fuel degradation follows the known routes for low-temperature oxidation of hydrocarbons [34,35]. The mechanism of oxidation of alkanes is quite general; the specificity of each system lays mostly in the *initiation stage*, where radical chains are generated by an external source of radicals of certain intensity measured with an *initiation rate* v_i [34,35]. This stage requires careful analysis when it comes to deposit formation. In particular, one must identify the nature of the initiator.

A common assumption in the literature is that the radical chain leading to fuel degradation is initiated by the dissolved oxygen [1,32,33]. In the lubricant literature, however, it has been established that the lubricant degradation is initiated by gas phase radicals transported through the quench layer and penetrating into the lubricant film [52-56]. It is posited here that the same mechanism plays a role in the degradation of the fuel film at the injector wall. Therefore, our first task is to investigate the possible radical chain initiators in the quench layer.

We used our quench layer model to shortlist the species that can initiate a radical chain in the fuel film. The two criteria for shortlisting were high concentration and high reactivity (data for the initiation rate of various initiators is available [35]; in most cases, we assumed that the ratio between the fuel film and quench layer concentration is of the order of 1, in the absence of data). The gas species we could identify as problematic are the following: NO_2, NO, $HO_2\cdot$, $CH_3\cdot$, $C_3H_5\cdot$, i-$C_4H_7\cdot$, $\cdot CH_2CHO$, $CH_3O\cdot$, $CH_3O_2\cdot$, $C_8H_{17}O_2\cdot$; O_2 was also considered. Among these species, the estimated rate of initiation was the highest for NO_2, significantly greater than the total contribution of all other species. The second most important initiator is O_2. Certain relatively reactive species present in the quench layer (such as $CH_3O\cdot$) contribute insignificantly to the initiation compared to NO_2 in part due to depletion (cf. S3).

In addition to NO_2, we found that nitric oxide NO also contributes significantly to the degradation process. From our quench layer model it follows that NO has quite high concentration near the injector surface at the considered stoichiometric conditions, especially near the pressure peak – the dependence on time during an engine cycle is shown in **Figure 2**-*left*. However, its role is not that of an initiator. We found no data for possible hydrogen abstraction reactions from the fuel hydrocarbons by NO. Therefore, we investigated other possible reactions discussed in the literature and found one that reaches a significant rate – this is $RO_2\cdot + \cdot NO \rightarrow RO\cdot + \cdot NO_2$, cf. e.g. [57,35]. This is essentially a branching step since it converts the peroxide radical, $RO_2\cdot$, which is not very reactive under the conditions in the fuel film, to a very reactive alkoxy radical $RO\cdot$.

The simulations suggest that late in the combustion stroke, the concentration of $\cdot NO_2$ in the quench layer is higher than that in the bulk of the cylinder, **Figure 2**-*right*. The excess $\cdot NO_2$ is produced from nitric oxide: as the latter is transported to the quench layer, it recombines with other radicals to form $\cdot NO_2$ and HNO_2 ($\cdot NO + HO_2\cdot \rightarrow \cdot NO_2 + HO\cdot$ and $\cdot NO + HO\cdot \rightarrow HNO_2$ [58]; a similar process produces $\cdot NO_2$ in the exhaust gases, e.g., *sec. 11.2.2* of Ref. [59]). In the relevant temperature range, according to our model, the quench layer concentrations of $\cdot NO$ and $\cdot NO_2$ are only weakly dependent on the wall temperature (apart from the trivial dilution effect due to $C \propto 1/T_{tip}$) – this is illustrated in Figure S3 in S1. Note that the quench layer has much higher concentration of O_2 than the cylinder (the simulated profiles are given in Figure S2 in S1) – $[O_2]$ remains high throughout the cycle as no combustion occurs in the quench layer and the time for exchange is long during the power stroke.

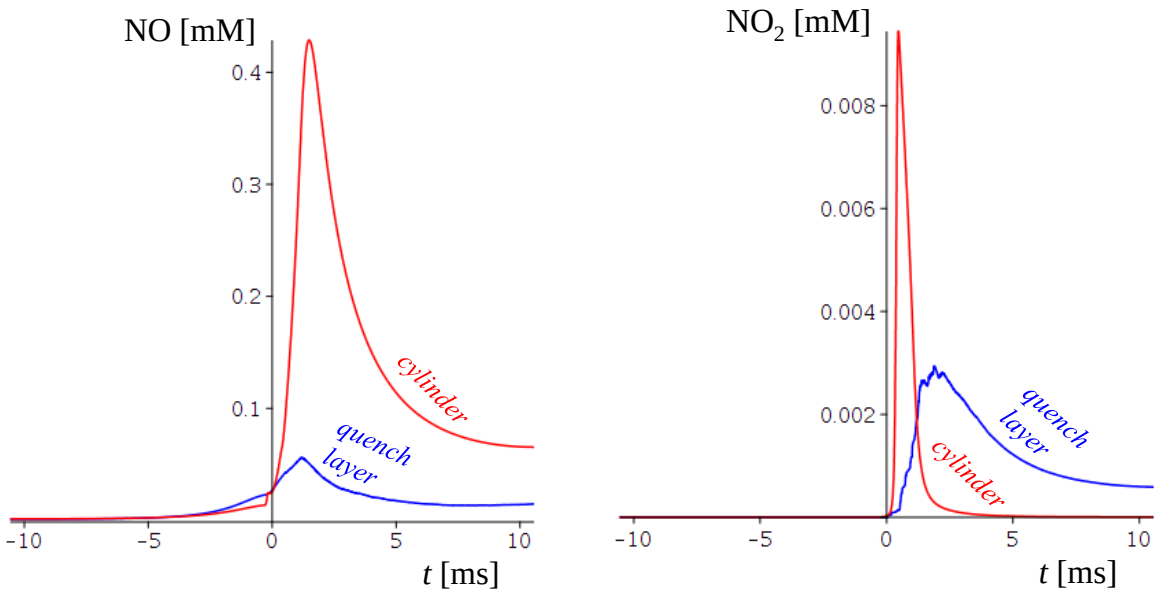

Figure 2: Simulated evolution of the concentration of nitric oxide (*left*) and nitrogen dioxide (*right*) in the quench layer at the injector surface (blue lines). The respective concentrations in the cylinder bulk are shown for comparison (red). T_{tip} = 160°C.

There must be a significant amount of the alkanes in the quench layer (as much as a mole fraction of 1 right next to the surface when the fuel is at its boiling temperature, cf. S3). The hydrocarbon vapours will dilute the gases in the quench layer, leading to decrease of $[O_2]$ and $[NO_x]$ there, which can slow down the degradation. On the other hand, the vaporized fuel in the quench layer will degrade itself, contributing to the deposition and compensating in part for the dilution effect. At the peak of the pressure (near which most of the degradation occurs), we expect both effects to be small and are thus neglected; the limitations of this approximation are analysed in S3. Another complication we neglect is that there exist other possible ways to initiate the oxidation. One mechanism that can be important for the deposits inside the nozzle channel is oxidation initiated by flow-induced shear stress (e.g., *sec. 1.10.1* in Ref. [60], [61]). The flow through the orifice causes significant heating of the fuel (the average increase of temperature is $\Delta T = \Delta p/c^F\rho^F$ [62], where c^F is heat capacity per unit volume of gasoline and ρ^F is density; ΔT is of the order of 5-15 °C for gasoline injectors). If hydrodynamic cavitation develops, the heating will be highly inhomogeneous, with hot spots reaching hundreds of degrees, causing cracking and formation of radicals able to initiate radical chains [61]. While such a mechanism is plausible, it has an important peculiarity: cavitation-induced reactions have a characteristic negative temperature dependence of the degradation rate (the radical chain reaction rate is decreasing as temperature increases [61]). On the contrary, most studies on deposition report significant increase of the degradation rate with the increase of the temperature. Therefore, we did not consider the cavitation mechanism.

2.2 Degradation of the fuel film

The chemical pathways for low-temperature oxidative degradation of hydrocarbons are known in some detail [34,35]. A number of studies modelled the process with a focus on fuels [1,32,63,64]. However, we are not aware of any studies of fuel degradation under reciprocating engine conditions. There are major differences between a typical fuel degradation laboratory

test and the degradation of the fuel film at the nozzle tip under the violent conditions within the cylinder of a high-speed reciprocating internal combustion engine, summarized in **Table 1**.

For a gasoline film at the injector tip, the fuel temperature is in the range T^F = 90–190°C. The concentration of the oxidation products in the fuel at CAD_b, where the droplet boils away, remains well below 1% as the leaked fuel droplets have only few milliseconds to degrade – this is a first significant difference to laboratory tests, Table 1. The major radical species involved in this early stage of the liquid phase oxidation, apart from NO_x, are the alkyl radicals R·, the peroxide radicals RO_2·, and the alkoxy radicals RO· [34,35].

We consider the oxidation of an alkane that propagates through intermolecular reactions rather than through intramolecular [65-67] ones – i.e. we assume that the considered alkane does not have the structural component H-CR^1-CH_2-CR^2-H, where R^1 and R^2 are alkyl groups (this is valid for heptane and isooctane). The reactions we consider are:

$$\begin{aligned}
\text{i}\cdot + \text{RH} &\rightarrow \text{Hi} + \text{R}\cdot, && \text{“i” (initiation);}\\
\text{R}\cdot + \text{O}_2 &\rightarrow \text{RO}_2\cdot, && \text{“o” (oxidation of R·);}\\
\text{RO}_2\cdot + \text{RH} &\rightarrow \text{RO}_2\text{H} + \text{R}\cdot, && \text{“a” (propagation of RO}_2\text{·);}\\
\text{RO}\cdot + \text{RH} &\rightarrow \text{ROH} + \text{R}\cdot, && \text{“aOH” (propagation of RO·);}\\
\cdot\text{NO} + \text{RO}_2\cdot &\rightarrow \cdot\text{NO}_2 + \text{RO}\cdot, && \text{“NO” (branching by NO);}\\
2\text{RO}_2\cdot &\rightarrow 2\text{RO}\cdot + \text{O}_2, && \text{“OH” (formation of RO·);}\\
2\text{RO}_2\cdot &\rightarrow \text{termination products} + \text{O}_2, && \text{“t” (termination).}
\end{aligned} \tag{4}$$

By RH we denote the most reactive type of C-H bonds in the fuel film. Therefore, for n-alkanes and branched alkanes that do not contain tertiary C-atoms, [RH] is the concentration of the alkane times the number of secondary C-H bonds per molecule. For branched alkanes possessing tertiary C-atoms, [RH] is the alkane concentration times the number of tertiary C-H bonds per molecule (it must be valid that the tertiary C-H bonds are isolated, otherwise intramolecular propagation will contribute to the process [65,66]). For the considered mixture of isooctane and heptane, [RH] = 1×[C_8H_{18}], as the isooctane contains a single tertiary C-H.

Let us now consider the rates of the reactions (4), starting with the *initiation.* In the engine, there are several possible initiators: i· may stand for O_2, ·NO_2, HO_2· etc. Assuming that all of them react with RH according to the bimolecular reaction (4)-i, for the total rate of production of R· we obtain

$$v_\text{i} = \sum_\text{i} k_\text{i}[\text{i}\cdot][\text{RH}]. \tag{5}$$

The radical formation by O_2 may actually follow a third order rate law [35] (2RH + O_2 → 2R· + H_2O_2). In Eq (5), the film temperature (and therefore k_i) and especially [i·] are time-dependent (see Figure 1 & Figure 2) – this is a second major difference to laboratory conditions, cf. Table 1. Among the species in the quench layer, the nitrogen dioxide is by far the most important initiator. The rate of initiation by [O_2] (which is the one considered in the literature [1,32,33]) is much slower – using the rate parameters from Table S2 in S2, even if [NO_2]/[O_2] is of the order of 10^{-5} as it follows from our simulations, the initiation rate due to NO_2 is still hundreds of times larger ($k_{\text{i,NO}_2}$[NO_2] >> $k_{\text{i,O}_2}$[O_2] in the range 100-220°C). Initiation by [O_2] may become important only at elevated temperatures and lean mixtures, especially if fuel does not contain tertiary C-H bonds – but even in this case, the NO_2 initiation should normally dominate. In addition, according to Mayo et al. [63], O_2 is of decreased solubility in fuel at *T* higher than 190°C, complicating further the hypothesis for O_2-initiation.

Oxidation. The rate of the radical oxidation (4)-o is [34,35]:

$$v_\text{o} = k_\text{o}[\text{R}\cdot][\text{O}_2]. \tag{6}$$

The process is very fast, as long as O_2 is not depleted. Little depletion is expected in the quench layer (Figure S2 in S2) – there, O_2 is even of increased concentration due to compression.

Bulk intermolecular hydrogen abstraction, Eq (4)-a & aOH. Both major radical species present in the fuel, RO· and RO_2·, are able to propagate the radical chain by abstracting a hydrogen atom from a nearby hydrocarbon molecule:

$$v_a = k_a[RO_2\cdot][RH] \quad \text{and} \quad v_{aOH} = k_{aOH}[RO\cdot][RH]. \tag{7}$$

The propagation of the third radical R· ($R^1\cdot + R^2H \leftrightarrow R^1H + R^2\cdot$) has no effect on the process when a single hydrocarbon reacts (products are the same as the reacting species). However, it can have an equilibrating effect in case of mixture of HCs, which may be important for the deposition process. Seemingly, this reaction has not been studied in the literature, which might mean it is relatively slow. It is mentioned as a stage of the combustion of CH_4 by Emanuel' and Knorre [68].

Bulk termination: the reactions (4)-t & OH are simplified [34,35], but most parameters reported in the literature for the termination process refer to them. Their rates are:

$$v_t = k_t[RO_2\cdot]^2 \quad \text{and} \quad v_{OH} = k_{OH}[RO_2\cdot]^2. \tag{8}$$

Instead of k_{OH}, the a-parameter is often used (a measure of the ratio between the cage termination and cage alcohol propagation), related to the rate constants above as $k_{OH} = k_t(1 - a)/a$ (Table S2).

Finally, the *branching reaction* (4)-NO is of rate [57]:

$$v_{NO} = k_{NO}[RO_2\cdot][NO]; \tag{9}$$

as in most radical-radical reactions, it is only weakly dependent on the temperature.

The values of the rate parameters reported in the literature are, unfortunately, contradictory and the rate constants may vary by orders of magnitude depending on the source. A common mistake in the literature is the use of rate parameters referring to *one alkane molecule* together with parameters referring to *one reactive hydrogen atom* – for example, the values within a single table in Refs. [34,35] can refer to both definitions, without clear indication of which one is used. A second problem is the high percent of misquotations, vitiating the existing data collections. In Table S2, we collected relatively reliable data for the Arrhenius parameters of the reactions above (most of which are average values for several alkanes), that allow the calculation of the oxidation rate of normal and branched alkanes with sufficient accuracy for the aims of this work.

2.2.1 Gas transfer

The concentration of the relevant reactive species in the quench layer is related to the respective film concentration through Henry's law,

$$[i\cdot] = K_{H,i}[i\cdot]^G, \tag{10}$$

where [i·] is the concentration in the film (at the location of the interface fuel|gas, in case of bulk heterogeneity), $[i\cdot]^G$ is assumed to be the simulated quench layer concentration, and $K_{H,i}$ is Henry's constant of the species i·. Using this concentration in the rate laws above involves several serious approximations. First, a Fuchs layer may develop in certain cases. This would modify Eq (10) with a Hertz-Knudsen term (discussed in S3). The second approximation is the neglected concentration polarization of the quench layer (cf. S3). A third assumption is that the concentration [i·] is homogeneous – actually, the radical needs some time to diffuse through the liquid. This latter assumption will hold if the convective diffusion in the leaked droplet is fast enough. If the transport process was driven by pure diffusion, for the period between CAD_0 and CAD_b ($\tau_{degr} \sim 5$ ms), the diffusion length is $L_i \sim (D_i \tau_{degr})^{1/2} \sim 1$ μm, where D_i is the diffusion coefficient of i· in the fuel phase ($\sim 10^{-10}$ m^2/s). As L_i is small compared to the film thickness h^F, only a relatively thin portion of the film would have been saturated under these conditions. However, during the accumulation stage, a strong Marangoni flux develops, driving liquid from the hotter three phase contact to the colder evaporating free surface (we investigated a similar

process in Ref. [69]). The characteristic time of this flow is of the order of $\eta^F R^F/\sigma^F$ (R^F is size of the droplet, η^F and σ^F are the viscosity and surface tension of the fuel, respectively); its value is much less than ms for all reasonable values of these parameters, which means that the convective transfer from the surface to the bulk of the droplet is fast enough to equilibrate the distribution of i·, unless they are not extremely reactive, cf. S3.

The values of Henry's constants for the relevant gases and liquid alkane phase at the considered temperatures are not available in the literature, except for O_2 [35]. For Henry's constant of NO_x, we used the value $K_H = 1$, a rough estimate based on Refs [70,71]. Considering the approximate quench layer concentrations of $[NO_x]^G$ we use (see Sec. 2.1.3), the absence of precise data for K_H should be unimportant for the accuracy of our model, unless K_H has a significant temperature dependence – such a dependence may affect the trends of the rate vs. temperature dependence which we discuss in the following sections.

2.2.2 Evolution of the film composition during a cycle

Comparison of the reaction times with the period τ of the cycle (related to the engine speed as $\tau = 2/\nu$) would show that the assumption for quasi-steady state holds for the two more reactive radical species produced during the oxidation process, RO· and R·. However, this is not the case with the least reactive peroxide radical RO_2·. Actually, our analysis shows that, at the investigated conditions, $[RO_2\cdot]$ remains low and, as a result, the rates v_t and v_{OH} (which are proportional to $[RO_2\cdot]^2$, Eq (8)) are low compared to v_i. We will demonstrate this rigorously post factum, after solving the kinetic problem under the assumption for small $[RO_2\cdot]$ and using an iteration to test the assumption.

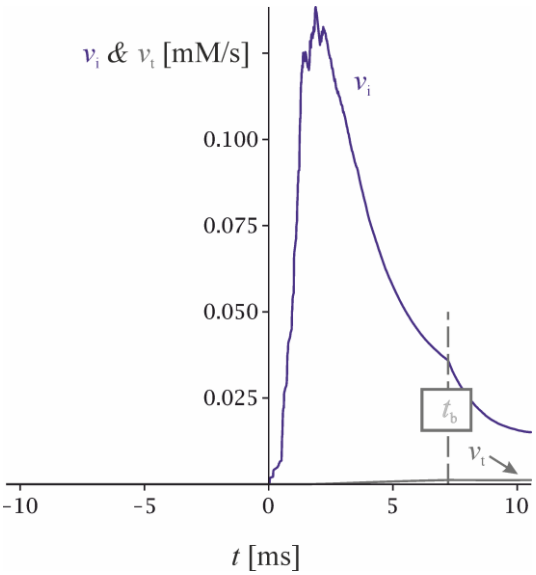

Figure 3: Initiation and termination rates in the film, v_i and v_t (blue and grey), as function of time t. Eqs (5),(8)&(14) were used (with initiation by NO_2). T_{tip} = 160°C. The comparison shows that $v_i >> v_t$, meaning that the oxidation is in accumulation (unsteady) regime with respect to RO_2·. After the boiling point t_b, the rate v_i has a cusp – before it, film's temperature is equal to T_{tip}, and after it – to T_b.

According to reaction scheme (4) with $[RO_2\cdot]^2$ neglected, the conditions for quasi-steady state for RO· and R· read

$$d[R\cdot]/dt = v_i + v_a + v_{aOH} - v_o \approx 0;$$
$$d[RO\cdot]/dt = v_{NO} - v_{aOH} \approx 0. \quad (11)$$

Substituting here Eqs (6)-(7), and solving for [R·] & [RO·], one obtains the relation of these concentrations to [RO_2·] and v_i:

$$[\mathrm{RO}\cdot] = \frac{k_{\mathrm{NO}}[\mathrm{NO}]}{k_{\mathrm{aOH}}[\mathrm{RH}]}[\mathrm{RO_2}\cdot];$$

$$[\mathrm{R}\cdot] = \frac{v_\mathrm{i} + \left(k_\mathrm{a}[\mathrm{RH}] + k_{\mathrm{NO}}[\mathrm{NO}]\right)[\mathrm{RO_2}\cdot]}{k_\mathrm{o}[\mathrm{O_2}]}. \quad (12)$$

The mass balance for RO_2· under the considered conditions reads:

$$\mathrm{d}[\mathrm{RO_2}\cdot]/\mathrm{d}t = v_\mathrm{o} - v_\mathrm{a} - v_{\mathrm{NO}} = v_\mathrm{i}, \quad (13)$$

where we used the first of Eqs (11). This rate is not zero, so accumulation regime holds for RO_2·. The concentration of the peroxide radical follows from the integration of Eq (13):

$$[\mathrm{RO_2}\cdot] = \int_{t_0}^{t} v_\mathrm{i}\mathrm{d}t\,, \quad (14)$$

where t_0 is the time at which the degradation process starts ($t_0 = \tau \times \mathrm{CAD_0}/720^\circ$). In contrast, in the steady laboratory regime, where $[\mathrm{RO_2}\cdot]^2$ is significant and $v_\mathrm{i} = 2v_\mathrm{t}$, one obtains for [$RO_2$·] the classical result [63,34,35]:

$$[\mathrm{RO_2}\cdot]_{\mathrm{st}} = (v_\mathrm{i}/2k_\mathrm{t})^{1/2}. \quad (15)$$

The initiation rate v_i is calculated via Eq (5) (with i· ≡ NO_2) in **Figure 3**, using the rate parameters from Table S2, T^{F} for the temperature of the film and the simulated evolution of [NO_2] in the quench layer (Figure 2-*right*). The initiation rate follows the trend of the concentration [NO_2] in the quench layer and thus has a maximum near the cylinder pressure peak.

The initiation rate is further integrated according to Eq (14) to yield the concentration of RO_2· during a cycle – **Figure 4**, blue line. Using it, we can calculate the termination rate $v_t = k_t[\mathrm{RO_2}\cdot]^2$ on first iteration – it is given in Figure 3 (grey line). As seen, the validity of the assumption $v_t << v_i$ is confirmed. Thus, we reach another significant difference between laboratory conditions and cylinder (Table 1): in a bench test, RO_2· has enough time to accumulate and to react through the termination reaction (4)-t, resulting in a deposition process that is quasi-steady with respect to RO_2· (so Eq (15) is valid). If the process was following this regime, the concentration of RO_2· would be proportional to $v_i^{1/2}$, as shown in Figure 4, grey line. Instead, the time for accumulation of the quantity of RO_2·, needed for significant rate of termination, is of the order of tens of ms, longer than the period of the cycle. Therefore, [RO_2·] must be calculated using Eq (14) (accumulation regime). This difference results in completely different dependences of the total oxidation rate in the two regimes on T, v_i etc. At the end of the cycle, the radicals RO_2· are transferred to the proto-deposit phase (see Sec. 2.3.1 below), and with the next cycle, the whole process starts again – therefore, we refer to the engine-relevant regime as to *cyclic accumulation* of RO_2·.

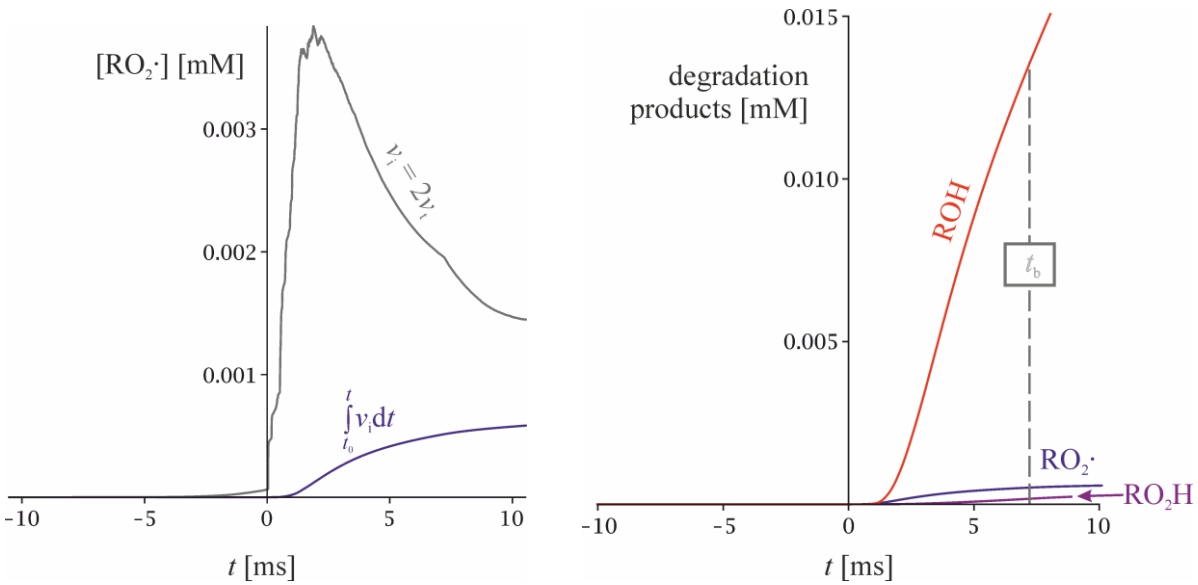

Figure 4: *Left* – concentration of $RO_2\cdot$ in the film vs. time. Blue line: cyclic accumulation regime, Eq (14); grey line: $[RO_2\cdot]_{st}$ that would hold if the steady-state regime were acting, Eq (15). T_{tip} = 160°C. *Right*: composition of the fuel film as a function of time.

Once $[RO_2\cdot]$ is known, one can proceed with the calculation of the concentration of the non-radical products of the reaction scheme (4). The rate of formation of the alcohol is equal to $d[ROH]/dt = v_{aOH}$, and that of the peroxide is $d[RO_2H]/dt = v_a$. Integration yields

$$[ROH] = [RH]\int_{t_0}^{t} k_{aOH}[RO\cdot]dt\,;$$

$$[RO_2H] = [RH]\int_{t_0}^{t} k_a[RO_2\cdot]dt\,, \qquad (16)$$

where Eqs (7) have been used and $[RO\cdot]$ is calculated via Eq (12). The evolution of the two concentrations during a cycle is given in Figure 4-*right*. As can be seen, the main product of the considered initial stage of the oxidation is the alcohol, and at the considered temperature, it reaches concentration of at most 0.02 mM (3 ppm) before the boiling point. The second most important product is the peroxide radical – in the accumulation regime, $RO_2\cdot$ has concentration that is higher even than that of the hydroperoxide RO_2H.

2.3 Rate of deposit formation

We investigate two mechanisms of deposition. The first one is relevant to the conditions at the injector tip, and involves solid particles (as Refs. [6,7] suggest). In this situation, we assume that the oxidized products accumulated in the fuel droplet are deposited at the injector surface once CAD_b is reached. The process involves:

(i) re-suspension of the deposit produced in the previous cycle by the fuel injection and the subsequent dribble;

(ii) adsorption of the oxidation products onto the extended surface of the suspension (i.e. *filtration* of the fuel by the suspended polar particles);

(iii) precipitation of the suspended particles after the droplet boils.

The nozzle channel deposits cannot be produced by such a mechanism as the solid particles will be swept off completely by the injection. In this case, we assume another scenario, where the slower process of direct oxidation of the interface deposit|fuel is responsible for the deposition.

2.3.1 Re-suspension-filtration-precipitation mechanism

The morphology of the tip deposits – involving small primary particles, aggregates, large voids [6] – suggests that the deposit particle formation occurs in the bulk of the fuel film. Direct nucleation and subsequent precipitation is hardly possible, as the oxidation products are of very low concentration (a few ppm, Figure 4) just before the point of boiling. A more consistent hypothesis is that the deposit left from the previous cycle is acting as a filter for the fuel, adsorbing the polar material produced by the oxidation. First, the droplet wets the porous deposit; the strong Marangoni flow during leakage then re-suspends the particles precipitated during the previous cycle. Once CAD_b is reached, most of the fuel vaporizes, bringing about an increase in the concentrations of the oxidation products and the suspended particles. Under such conditions, the solid particles adsorb the oxidation products, acting as a filter. At $CAD > CAD_b$, as V^F decreases to zero, the three phase contact line recedes toward the nozzle hole. The suspended particles precipitate near the three phase contact line, probably following the coffee ring mechanism [72]. Possibly, a fraction of the particles is transferred inside the nozzle channel, but we neglect this. During the period where the surface is dry, the newly adsorbed material ages and degrades further (e.g., under the action of the $RO_2\cdot$ radicals). Such a mechanism provides an explanation for the observed co-existence of fresh and aged material in the tip deposits [6]. It also gives good grounds for understanding the mechanism of action of the fuel anti-deposit additives [8,24,73], which, by functionality, are dispersants.

If this re-suspension-filtration-precipitation mechanism is followed, one can assume that the amount of deposit produced in each cycle is approximately equal to the amount of oxidized products formed in the droplet until CAD_b is reached. The early oxidation products (ROH, $RO_2\cdot$, and RO_2H) separate as a polar phase (*proto-deposit*), adding mass to the pre-existing deposit each time the leaked droplets vaporize. We assume also that the reactions which occur in the polar proto-deposit phase as it ages do not lead to a significant change of the deposit volume (neglecting the possible gasification process and the addition of lubricant-derived material). The number of moles of deposit precursors formed during one cycle is given by $n^D = V^F([ROH] + [RO_2\cdot] + [RO_2H])|_{t=t_b}$, or per unit area, $n^D/A^D = h^F([ROH] + [RO_2\cdot] + [RO_2H])|_{t=t_b}$. Here, $h^F = V^F/A^F$ is the average thickness of the fuel film (fuel volume/covered area of the injector surface, ~100 μm). If the average molar mass of the deposit precursors is M_d (about equal to the molar mass of ROH) and the density of the deposit is $\rho^D \sim 300$ kg/m^3 (porous carbonaceous material), then, upon each cycle, the thickness of the deposit layer increases by

$$\Delta h_{tip} = \frac{M_d}{\rho^D} h^F \left([ROH]+[RO_2\cdot]+[RO_2H]\right)_{t=t_b}. \qquad (17)$$

For the three concentrations in the brackets, Eqs (14)&(16) are used. Thus, the increase of the deposit thickness is proportional to the amount of fuel leaking out of the nozzle (h^F) and the concentration of deposit precursors produced until the point of boiling.

Dividing Δh_{tip} by the period τ of the cycle we obtain the average rate of deposit formation for the considered mechanism, illustrated in **Figure 5** (isooctane is in green), as a function of the tip temperature. The dispersion is due to the stochastic nature of our simulations. Note that Δh_{tip} produced per cycle can hardly be constant for hours (despite the units we chose for the figure) – the formation rate changes as the deposit builds up, because the carbonaceous layer insulates the injector wall and leads to increased wall temperature (Sec. 3.2 below). In addition, Eq (17) is giving the formation rate only. Deposit is also removed from the wall by various processes, which normally limit the thickness to a certain stationary thickness [50,19,22] – see Sec. 2.3.3.

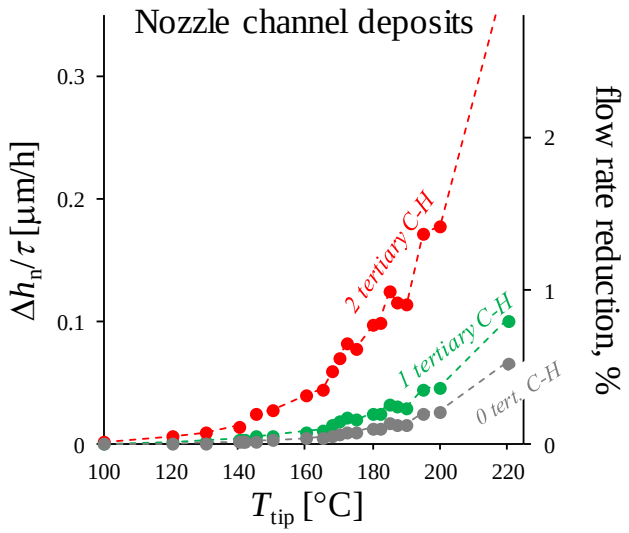

Figure 5: Rate of deposit formation at the injector tip (cycle-averaged) as a function of the tip surface temperature. For the effect of the alkane structure, 2,5-dimethylhexane (2 tertiary C-H bonds), isooctane (1 tertiary C-H) and 3-ethyl-3-methylpentane (0 tertiary C-H) are compared.

Let us now consider the effect of the chemical structure of the alkane components in the fuel on the deposition rate. The difference between thermal stability and oxidative stability of a fuel component is noteworthy: thermally stable HCs are often easily oxidized [74], and from practice it is known that gasoline containing more branched alkanes (increasing the octane number) actually causes worse deposits. This is, at least in part, due to the increased number of tertiary C-H bonds that are easy to oxidize. The mechanism above allows one to give a quantitative expression of this phenomenon, and use the values of the deposition rate to evaluate the propensity of various HC components in the fuel to form deposits.

We consider three octane isomers as examples for alkanes: 3-methyl-3-ethylpentane, containing no tertiary C-H bonds; isooctane, containing one tertiary bond; and 2,5-dimethylhexane, containing two isolated tertiary bonds. We have chosen these alkanes as they all have high octane number (so a similar combustion process and flame speed are expected), and very similar viscosity, surface tension, vapour pressure and density (ensuring similar spray characteristics and leakage rates), while having completely different rates of autooxidation. We assume that the combustion of these species (mixed with 5 *w*% heptane) leads to the same quench layer composition as in Figure 2. The tip deposit formation rate will be affected by their structure: the 2,5-dimethylhexane is oxidized twice as fast as the isooctane, due to the additional tertiary C-H bond. Therefore, 2,5-dimethylhexane has values of Δh_{tip} twice as high as those for isooctane, cf. Figure 5-red line. The 3-methyl-3-ethylpentane is oxidized only through its six secondary bonds, for which the hydrogen abstraction is slow (Table S2). The result is that this compound has the slowest tip deposit formation rate (Figure 5-grey line). In the following section, we will show that the rate differences are even more pronounced with the nozzle deposit formation rate.

2.3.2 Surface oxidation-adsorption mechanism

Any suspended particles in the fuel trapped inside the nozzle channel will be swept by the next injection. Therefore, the nozzle channel deposits must form through another mechanism. Our hypothesis is that deposition occurs through direct growth at the deposit|fuel interface, proceeding in two steps: surface oxidation and addition of polar degradation products via adsorption (cf. Figure S4 in S2).

To model the oxidation of the surface of the deposit, we first make the hypothesis that all reactions that are possible in the bulk of the fuel are also possible, in principle, at the polar deposit|fuel interface. This seems plausible, in view of the chemistry of this interface. The amphiphilic molecules (ROH, RO_2H) at the interface must be oriented with the polar head group toward the polar deposit phase, and with the hydrocarbon tail toward the fuel. Thus, on the fuel side, the interface deposit|fuel will be dominated by CH, CH_2 and CH_3 groups. Let the surface concentration of the reactive C-H bonds be [sH], where "s" indicates *surface site*. A deposit-bound C-H bond can react with the radical species dissolved in the fuel, following the reactions similar to those in the bulk phase, Eq (4). Thus, the attack of the radicals $\cdot NO_2$, $RO_2\cdot$ & $RO\cdot$ will result in hydrogen abstraction and formation of a surface-bound alkyl radical s·:

$$\begin{aligned} sH + \cdot NO_2 &\rightarrow s\cdot + HNO_2, & v_i^S &= k_i^S[NO_2][sH]; \\ sH + RO_2\cdot &\rightarrow s\cdot + RO_2H, & v_a^S &= k_a^S[RO_2\cdot][sH]; \\ sH + RO\cdot &\rightarrow s\cdot + ROH, & v_{aOH}^S &= k_{aOH}^S[RO\cdot][sH]. \end{aligned} \qquad (18)$$

Here, k_i^S, k_a^S & k_{aOH}^S are rate constants that are the surface equivalent of the respective k_i, k_a and k_{aOH} in the bulk. It can be assumed that k_x^S has a value of the same order of magnitude as that of the respective k_x in the bulk (where "x" stands for i, a or aOH), provided that the same type of C-H bonds take part in the reaction – we present some arguments for this conjecture in S2. Once the hydrogen is abstracted from the surface site, s· is oxidized to form a polar site (peroxide or alcohol, sO_2H or sOH):

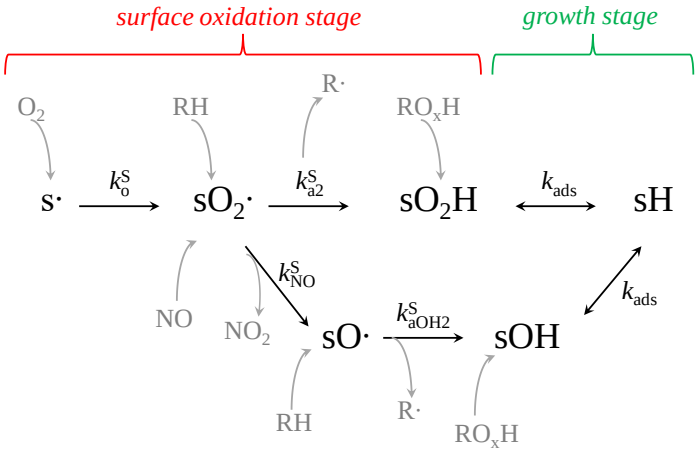

(19)

All steps but the last one are surface analogues of a respective bulk reaction in Eq (4). In the last step, an oxidized molecule from the fuel film *adsorbs reversibly* to the surface polar site, resulting in the growth of the deposit and the regeneration of the hydrophobic site sH ($sO_xH + HO_xR \leftrightarrow sO_xH\text{---}HO_xR$, which is equivalent to sH). Note the difference between k_a^S (that refers to the reaction between $sH + RO_2\cdot$) and k_{a2}^S (that refers to $sO_2\cdot + RH$): different CH bonds may be involved in these two reactions. The whole process can be divided in three steps: surface initiation ($sH \rightarrow s\cdot$), surface polar site formation ($s\cdot \rightarrow sO_xH$) and the growth step $sO_xH + HO_xR \rightarrow sH$. The overall "deposit formation" reaction is $sH + O_2 + RO_xH \rightarrow sH$. A schematic of the process is given in Figure S4. An alternative of the last step in Eq (19) is for *irreversible adsorption* to occur by a surface termination reaction, e.g., $sO_2\cdot + RO_2\cdot \rightarrow sO_2R + O_2$, where sO_2R is again equivalent to sH. Note that in the case of reversible adsorption, in order for the deposit to continue growing, one must assume that at certain stage during aging the reversibly adsorbed oxidation products react further to form irreversibly bound species.

An outstanding issue is the possibility for the exchange reactions $s\cdot + RH \leftrightarrow sH + R\cdot$; unlike the respective bulk equivalent, the outcome of this process is not trivial. An analysis of the possible effect from it is presented in S2.

As the hydrogen abstraction is a very slow reaction, it can be assumed that the rate-determining process in the scheme (18)-(19) is the surface initiation (18). Under this assumption, the rate of the overall process of addition of RO_xH to the surface is $v_{ads} = v_i^S + v_a^S + v_{aOH}^S$. Using Eqs (18)&(12), one obtains:

$$v_{ads} = \left\{ k_i^S[NO_2] + \left(k_a^S + \frac{k_{aOH}^S k_{NO}}{k_{aOH}[RH]}[NO] \right)[RO_2\cdot] \right\}[sH]\,. \qquad (20)$$

For alkanes that have several tertiary bonds, we can assume that $k_x^S \approx k_x$ (both constants refer to the rate parameters of tertiary RH in Table S2). The same assumption can be made for the case of no tertiary atoms in the molecule (but with the rate parameters from Table S2 for secondary atoms). However, for isooctane (1 tertiary atom), the degradation products that adsorb, e.g., isooctanol, have hydrophobic chain that does not contain tertiary C-H bonds. In this case, the bulk abstraction constant k_{aOH} in Eq (20) refers to the tertiary bond of the isooctane, but the surface abstraction constants k_i^S & k_{aOH}^S should refer to its secondary bonds. Finally, for isooctane, the rate constant k_a^S should refer to a tertiary $RO_2\cdot$ radical (isooctylperoxy radical) attacking a secondary C-H at the deposit surface, cf. S2.

The concentrations $[NO_2]$, [NO] and $[RO_2\cdot]$ in Eq (20) are those in Figure 2 & Figure 4. For [sH] we assume the value

$$[sH] = x_{active} r_W / N_A a_{sH}; \qquad (21)$$

here r_W is the ratio between the actual area of the rough deposit surface and the projected area – known as the Wenzel factor in the colloid field [75], and is a measure of the surface roughness. We assume the value $r_W = 10$ for it, typical for porous materials. For the *area per C-H bond* a_{sH} at the interface of the deposit, we assume a value similar to the one at the surface of an alkane – about 10 Å^2. The quantity x_{active} stands for the fraction of reactive C-H bonds at the surface among all C-H bonds. For isooctane, the surface of the deposit is assumed to be covered by the tertiary isooctanol, which has 5 CH_3 groups and 1 CH_2 group; therefore, the fraction of the more reactive secondary C-H bonds is $x_{active} = 2/17$. N_A is Avogadro's number.

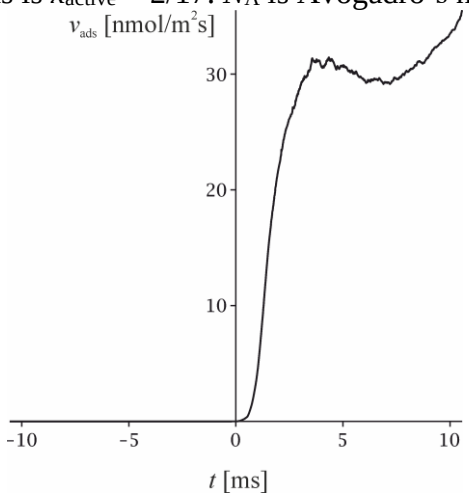

Figure 6: Deposit formation rate in the nozzle channel as a function of time during the compression and power strokes, according to Eq (20). Isooctane, $T_{tip} = 160^\circ$C.

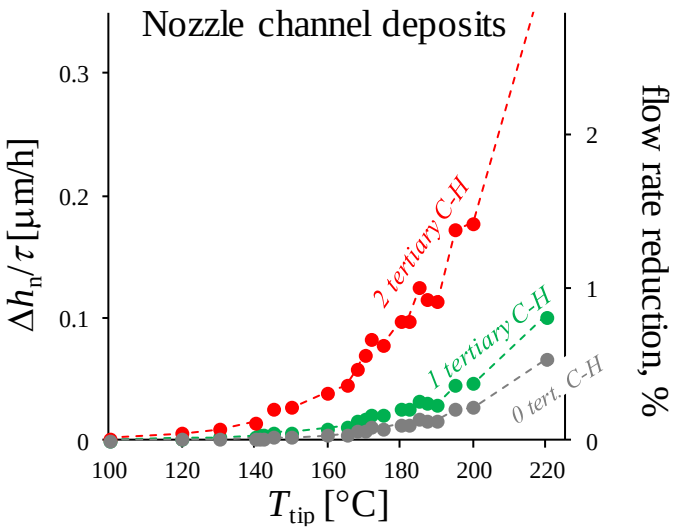

Figure 7: Average rate of deposit formation via the surface oxidation-adsorption mechanism in the nozzle channel as a function of the injector wall temperature, according to Eq (22). The right ordinate axis corresponds to the flow reduction percentage due to the deposit, which is proportional to v_n, see Sec. 3.1.

The change of the adsorption rate during a cycle is calculated in **Figure 6**. For the considered case, the leading term in Eq (20) is the one proportional to [NO]. Unlike the tip deposits, we assume that the nozzle deposit accumulation continues after the point of boiling, as it is unlikely that the fuel in the nozzle vaporizes completely at CAD_b (the nozzle is constantly fed by fresh leaked fuel). The accumulated deposit during a whole cycle is:

$$\Delta h_n = \frac{M_d}{\rho^D} \int_{t_0}^{t_{end}} v_{ads} \mathrm{d}t \,, \tag{22}$$

where t_{end} denotes the end of the combustion stroke. Dividing Δh_n by τ, we obtain the cycle-averaged rate of deposit formation in the nozzle channel. The result is illustrated in **Figure 7** (isooctane is in green).

We further considered the relation between nozzle channel deposit formation rate and the alkane structure, on the example of the same 3 alkanes analysed in Figure 5 (where their tip deposit propensity was investigated). We assume the following values of the relevant structural parameters in Eqs (20)-(22). For the least reactive 3-methyl-3-ethylpentane, the fraction of secondary bonds at the surface is x_{active} = ¼ and all rate constants in Eq (20) refer to secondary C-H bonds. The result for the rate $\Delta h_n/\tau$ is the grey line in Figure 7. For the isooctane, the surface of the deposit is actually relatively passive, since the single tertiary bond of i-C_8H_{18} is already oxidized to produce the adsorbed species and the surface oxidation process can be initiated only via the secondary C-H bonds. For this reason, with regard to the nozzle channel surface oxidation-adsorption mechanism, the isooctane is predicted to be of similar deposit propensity to that of the 3-methyl-3-ethyl pentane (compared to their rather different $\Delta h_{tip}/\tau$ values in Figure 5). In contrast, a deposit made by 2,5-dimethylhexane degradation products grows significantly faster, as the surface has a fraction x_{active} = 1/17 of tertiary bonds (note that, for the values of $\Delta h_n/\tau$ for 2,5-dimethylhexane in Figure 7, we added the initiation rate due to H-abstraction via the 4/17 fraction of secondary C-Hs, since it is not negligible).

Let us remark here that the outcome of the surface oxidation is the transformation of the initial oxidation products (ROH, RO_2H) to bifunctional species at the interface deposit|fuel. This polyfunctionality means ability to polymerize [60] – and the aging processes definitely involve polymerization. This is the reason why the most dangerous octane isomer in the fuel identified via the value of the deposition rate in the channel contains two tertiary C-H bonds.

Similarly, alkanes that are able to react through an intramolecular propagation mechanism will form polyfunctional products already in the bulk. The adsorption of such a product will immediately create a polar site (cf. Figure S4-*right*). For example, a likely product of the intramolecular oxidation is the alcohol-peroxide HO_2ROH [34,66]; it can adsorb at a polar surface site via sOH + HO_2ROH ↔ sOH---HO_2ROH ~ sOH. In such a case, the slow surface initiation step is skipped. Thus, alkanes containing the structural element H-CR^1-CH_2-CR^2-H can be expected to have higher propensity for deposit formation than those with isolated tertiary bonds.

Eq (22) involves several major approximations. The concentration of the oxidation products and NO_x in the fuel before CAD_b must be lower in the nozzle compared to the tip, due to the increased diffusion length; lower temperature can also be expected. In addition, leakage feeds the base of the nozzle with fresh cold fuel, diluting the reactive species. On the other hand, late in the cycle, as the leaked droplet boils and retreats to the nozzle hole, the reaction volume decreases significantly yielding the opposite effect – in the time interval between t_b and t_{end}, the concentration of [RO_2·] in the nozzle channel is probably increasing. The exhaust and intake strokes may also contribute to the deposition in the channel [1]. The modelling of these effects requires better understanding of the leakage process and of the deposition of oxidized products at the tip during boiling. We use Eqs (22) as an order of magnitude estimate, hoping that the above effects cancel each other.

2.3.3 Experimental determination of the rates of deposit formation and removal

The process of removal of the deposits [19,22] is largely unrelated to their formation, and is a matter of a different study, yet one has to account for it when dealing with the experimental data. Two different mechanisms for the deposit removal should act at the tip and in the nozzle. The deposit in the channel is removed mechanically, by the turbulent shear stress during each injection [50]. The deposit at the tip, on the other hand, is rather thick and leads to thermal insulation of the injector surface, and therefore, to increased surface temperatures (Sec. 3.2 below). At high temperature [76], and especially in the presence of certain catalysts [77], gasification of the deposit occurs. Probably, a number of other mechanisms are also operating [19], in particular, removal via flaking and cracking [18] is likely.

Let us give an example of the effect of the removal rate on the deposition, limiting ourselves to a discussion on the empirical result of Aradi et al. [50] who showed that their experimental data for the decrease of the fuel discharge through the nozzle agree with the following rate law:

$$\mathrm{d}h_n/\mathrm{d}t = v_n - k_r h_n; \tag{23}$$

here, v_n is the rate of deposit formation and $k_r h_n$ is the rate of deposit removal. Both v_n and k_r are empirical quantities in the model of Aradi et al. Our surface oxidation-adsorption model in Sec. 2.3.2 indeed predicts that the rate of formation is independent of h_n, thus confirming the hypothesis of Aradi et al., and we can calculate v_n as

$$v_n = \Delta h_n / \tau, \tag{24}$$

where Δh_n is the increment of the deposit thickness per cycle due to the surface oxidation, Eq (22), and τ is the period of the engine cycle. The solution to Eq (23) for $h_n(t)$ is given by:

$$h_n = \frac{v_n}{k_r}\left(1 - \mathrm{e}^{-k_r t}\right) . \tag{25}$$

In order to compare the experimental results from Ref. [50] with our calculated deposit formation rates, we re-evaluated all data of Aradi et al. in Table S3 in S4 (we had to correct a small mistake in the regression data presented in *table 5* of [50], as explained in S4). The value of the nozzle radius is required for the determination of the absolute value of v_n; such was not

provided in [50], therefore, we assumed R_n = 50 μm (as for the real engine we are modelling). Aradi et al. studied the effect of the fuel formulation on k_r and v_n at T_{tip} = 173°C. The order of magnitude of v_n that follows from their data is in the range 0.9-1.6 μm/h for non-additized fuels (cf. S4). As for the removal rate constant k_r, its value is in the range 0.4-0.6 h^{-1} for non-additized fuel. We also processed data by Jiang et al. [78] for the change of the injector pulse width at fixed injected mass, which is also directly related to the orifice deposit thickness, cf. Sec. 3.1 and S4; their measurements correspond to v_n = 0.23 μm/h and k_r = 0.3 h^{-1} (using R_n = 80 μm from their *fig. 6*). In comparison, our model predicts deposit formation rate of ~0.07-0.1 μm/h for the most reactive octane isomer at 170-180°C. The difference between the predicted value and those found from the analysis of the engine experimental data is due to the alkenes and arenes present in the real fuels: the data in Refs. [50,78] refer to gasolines with 13-20% alkenes or 30-35% arenes. In addition, two of the fuels contain sulfur, which seems to show some anti-oxidant effect [79] resulting in an induction period for the autooxidation.

3 Effect of the deposits on the injector performance

Investigations of the effect of injector deposits on the injector performance and thermal conditions are scarce [8,17,80-82]. As a result, the mechanism of their adverse action is not completely understood. The best studied effect of the nozzle channel deposits seems to be the restricted fuel flow through the nozzle [8,17], which we consider briefly in Sec. 3.1. In Sec. 3.2, we investigate an effect of the tip deposits that can be readily analysed theoretically: the alteration of the injector wall temperature by the deposit layer. A third well-studied effect is the spray distortion [9,11,47,78] (including the increase of the mean droplet radius and the spray penetration, and the alteration of the spray angle), which, however, is not expected to have a dramatic effect in DISI engines with early injection timing. The distortion could have impact on the combustion process under cold-start conditions when the fuel is injected late into the combustion chamber, when the piston is close to TDC.

3.1 Nozzle channel deposits and channel plugging

The deposits in the nozzle alter the cross-section of the nozzle channel and lead to decreased discharge. The Reynolds number of the nozzle flow is of the order of Re ~ 10000-100000 (assuming R_n ~ 50-100 μm, Δp = 100-300 bar, ρ^F = 700-800 kg/m^3, η^F = 0.2-0.5 mPa·s, cf. Eq. (58) in S4); in this range, Bernoulli's equation can be used in the form [62]:

$$Q = C_d \pi \left(R_n - h_n\right)^2 \sqrt{2\Delta p / \rho^F} \,. \tag{26}$$

Here, R_n is the nozzle radius in the absence of deposits, Δp is the pressure drop across the nozzle, ρ^F is the density of the fuel, and C_d is the discharge coefficient. In general, C_d depends on both the channel geometry and the mean roughness ε of the wall. The nozzle channel deposit affects both R_n and ε, probably with non-monotonic combined effect on Q.

Aradi et al. [50] proposed the use of the reduction of the flow rate $1 - Q/Q_0$ as a measure of the deposit thickness. Indeed, in the case where $h_n << R_n$, a linear relationship holds between the two quantities. The linear formula can be derived by expanding Eq (26) into series at $h_n << R_n$. The result is:

$$1 - \frac{Q}{Q_0} = \left(\frac{2}{R_n} + \frac{\partial \ln C_d}{\partial R_n} - \frac{\partial \ln C_d}{\partial \varepsilon} \frac{\mathrm{d}\varepsilon}{\mathrm{d}h_n} \right) h_n \approx \frac{2h_n}{R_n} \,. \tag{27}$$

The factor $2/R_n$ is related to the proportionality of Q to $(R_n - h_n)^2$ for the turbulent flow, see Eq (26). The dependence of C_d on h_n is unclear: according to Colebrook-White equation [83], the derivative $\partial \ln C_d / \partial R_n \approx 0.5/R_n$, but using the correlation of Shapiro et al. [84,62], it is 0.05-0.1/R_n, cf. S4. As for the ε-term in Eq (27), the roughness will decrease dramatically as the first deposits grow inside the grooves of the steel wall, but once they are homogeneous, the deposit|fuel interface can be expected to be of relatively constant roughness so $\mathrm{d}\varepsilon/\mathrm{d}h_n \approx 0$. Curiously, from here it follows that a brand new injector could require certain time for deposits to accumulate in the grooves before maximum flow capacity is achieved. Neglecting the last two terms in Eq (27), i.e. assuming that $Q \propto (R_n - h_n)^2$ as Aradi et al. did [50,85], we obtain the approximate $1 - Q/Q_0 \approx 2h_n/R_n$.

The substitution of Eq (25) for $h_n(t)$ in Eq (27) yields the reduction of the discharge rate as function of t due to the accumulation of the deposits. For its limit at large times ($k_r t >> 1$), one obtains:

$$1 - \frac{Q}{Q_0} = \frac{2v_n}{R_n k_r}\left(1 - \mathrm{e}^{-k_r t}\right) \xrightarrow{t >> 1/k_r} \frac{2v_n}{R_n k_r} \ . \tag{28}$$

Thus, the reduction of the flow rate at $t >> 1/k_r$ is proportional to v_n/k_r. Assuming further that $k_r \approx 0.5\ \mathrm{h}^{-1}$ (see Table S3) independently of the temperature, we can draw the reduction of the flow rate as function of the wall temperature using the results for v_n from Sec. 2.3.2. According to Eq (28), $1 - Q/Q_0 \propto v_n$, therefore, we can use the second ordinate axis placed on the right side of Figure 7 to draw the result. The trend compares qualitatively well with the measured reduction in *fig. 3* of Kinoshita et al. [7]. As in the case of the data of Aradi et al., our calculated rates for alkanes are several times smaller than the experimental ones from Ref. [7]. This is unsurprising: real fuels were used in both Refs. [7,50], that contain HC species more reactive than alkanes.

Signal width τ_{signal} at fixed total amount $m_{injected}$ of injected fuel per injection can also be used to determine the rate of formation and removal. If $(\tau_{signal} - \tau_{lag})\rho^F Q = m_{injected}$ is constant, we obtain from Eq (28) the relation

$$\tau_{signal} = \tau_{lag} + \frac{m_{injected}}{\rho^F Q} = \tau_{lag} + \frac{\tau_{signal,0} - \tau_{lag}}{1 - 2h_n / R_n}, \tag{29}$$

where $\tau_{signal,0}$ is the unperturbed signal length and τ_{lag} is the injection time lag (due to the finite time needed to actuate the injector). Expanding this result into series for $h_n << R_n$ and substituting h_n with Eq (25),

$$\tau_{signal} = \tau_{lag} + \left(\tau_{signal,0} - \tau_{lag}\right)\left[1 + \frac{2v_n}{R_n k_r}\left(1 - \mathrm{e}^{-k_r t}\right)\right]; \tag{30}$$

here, we assumed that the time lag is unaffected by the presence of deposits (which should be approximately true for external injector deposits). We used this equation to determine v_n and k_r from the data of Jiang et al. (*fig. 7* in Ref. [78]), cf. S4 and Sec. 2.3.3.

3.2 Injector tip deposits and wall temperature

Nozzle temperature is a major factor in the deposition process [7,8], as discussed already in Sec. 2.1.2, 2.3.1 & 2.3.2. It is correlated with the inlet air and fuel temperatures, engine speed and load [17], but another major influence is the thickness of the deposit layer at the wall (compare to other engine deposits, e.g. [86]). The *average* temperature $\overline{T}_{tip}$ of the injector surface increases as the tip deposits accumulate and insulate the injector. Another significant effect, which, to our knowledge, has not been considered in the literature, is that the deposit insulation leads also to a dramatic increase of the temperature variations during each cycle.

Let a deposit layer of thickness h_{tip} exist between the hot combustion gases and a metal layer of thickness h^M; the outer wall of the metal is fixed to a temperature T_{out}. The interface metal|deposit is located at $z = 0$, and the deposit|air is at $z = h_{tip}$. The interface deposit|air is subject to a time dependent heat flux $q^S(t)$. This heat flux from the chamber to the injector wall is an output of the SRM Engine Suite software (based on Woschni's correlation [59]; the dependence of q^S on time is illustrated in Figure S7 in S5). It is a periodic function of period τ (twice the reciprocal of the engine rotational speed). The values of $q^S(t)$ during the exhaust and the intake strokes are estimated roughly: it is assumed that $q^S(t) = q^S(-180\ \text{CAD})$ from -360 to -180 CAD, and $q^S(t) = q^S(180\ \text{CAD})/2$ from +180 to +360 CAD (the precise profile in this range of CA degrees has little effect on the final results for the wall temperature).

The surface temperature that corresponds to $q^S(t)$ in Figure S7 can be found using the Fourier series technique [87,59]. The evolution of the temperature profile, $T(z,t)$, in the deposit and in the metal during the cycle is the solution to the one-dimensional heat transfer equation $\partial T/\partial t = \chi \partial^2 T/\partial z^2$ for the two layers, subject to boundary conditions **(i)** $T^M|_{z=-h^M} = T_{out}$, **(ii)** $\kappa^D \partial T^D/\partial z|_{z=h_{tip}} = q^S(t)$, and **(iii-iv)** continuity of T and the heat flux at $z = 0$. Here, χ is the thermal diffusivity of the metal or the deposit, related to the heat conductivity κ as $\chi = \kappa/c$, where c is the heat capacity per unit volume of the metal or the deposit. The solution to this problem is derived in S5. In particular, for $\overline{T}$ it is valid that:

$$\overline{T}^M = T_{out} + \frac{\overline{q}^S}{\kappa^M}\left(z + h^M\right) \quad \text{and} \quad \overline{T}^D = \overline{T}_{tip} + \frac{\overline{q}^S}{\kappa^D}\left(z - h_{tip}\right), \tag{31}$$

where $\overline{q}^S$ is the average heat flux to the wall (0.156 MW/m^2 for the data in Figure S7) and $\overline{T}_{tip}$ is the average surface temperature, given by the expression

$$\overline{T}_{tip} = T_{out} + \frac{h^M}{\kappa^M}\overline{q}^S + \frac{h_{tip}}{\kappa^D}\overline{q}^S . \tag{32}$$

$\overline{T}^M$ & $\overline{T}^D$ given by Eqs (31)-(32) (the 0th Fourier coefficients of $T^M(t)$ and $T^D(t)$) set the time-averaged profile of the temperature. Assuming that $\overline{q}^S$ is not strongly dependent on the injector wall temperature, we can use Eq (32) to predict immediately the effect of the deposit layer on the wall temperature: it corresponds to an increase by $\Delta T_{tip} = h_{tip}\overline{q}^S/\kappa^D$. Using the values κ^D = 2.5 W/Km [86] and $\overline{q}^S$ = 0.156 MW/m^2, we obtain an increase of the surface temperature of $\overline{q}^S/\kappa^D$ = 6.2 K per 100 μm deposit.

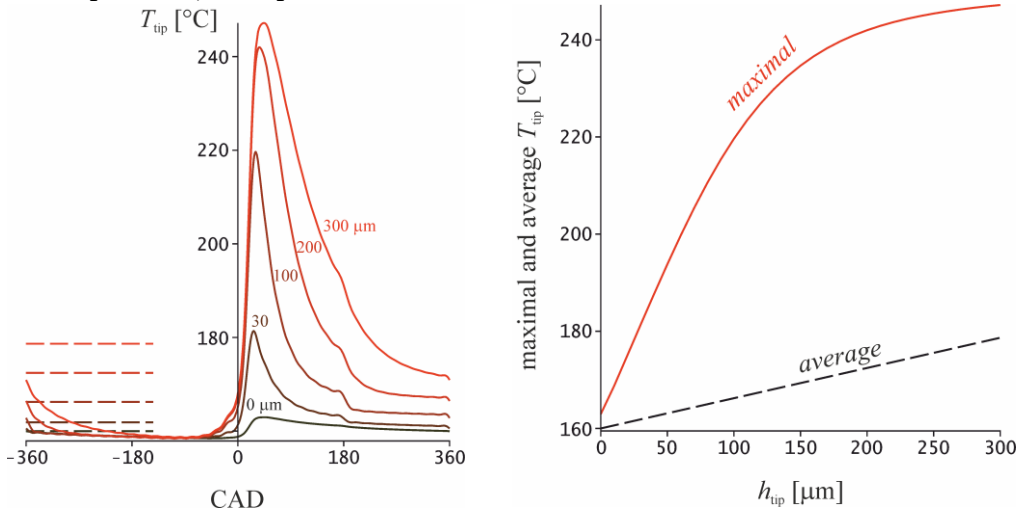

Figure 8: *Left* – wall temperature in the presence of deposit during a cycle at various values of h_{tip}. The dashed lines indicate the respective $\overline{T}_{tip}$. *Right*: dependence of the average (black dash) and the maximal wall temperature (red solid) on the thickness of the tip deposit.

The time-dependent terms in the Fourier expansion of the temperature profile (Eq (66) in S5) do not contribute to the average T. They allow, however, the evolution of the temperature profile during a cycle to be calculated. The whole profiles of T^{D} & T^{M} are considered in S5. Here we discuss only the time evolution of the surface temperature $T_{tip}(t)$ (obtained by setting $z = h_{tip}$ into Eq (66) in S5). It is plotted in **Figure 8**-*left* for several values of the thickness h_{tip}, using the following parameter values: average temperature of the metal surface 160°C; $\chi^{D} = 11.6\times10^{-6}$ m^2/s (assuming heat capacity as for coke); $\kappa^{M} = 54$ W/Km and $\chi^{M} = 15.3\times10^{-6}$ m^2/s as for iron [59]. As seen in the figure, in the absence of deposit, the wall temperature does not change significantly with time (T_{tip} = 160±2°C, grey line). A relatively thin tip deposit of thickness 30 μm increases the average temperature by less than 2°C. However, the amplitude of the oscillations around the average increases significantly – the maximal temperature reaches 181°C, which is an increase by ~20°C compared to the one of the clean injector surface. The maximal temperature continues to increase about linearly with h_{tip}, until deposit of thickness of the order of 150-200 μm is accumulated (**Figure 8**-*right*). After this, a plateau is reached, corresponding to the characteristic amplitude (≈ ±40°C) of the oscillations of T_{tip} at the surface of a thick deposit, where "thick" means $h_{tip} \sim 2\chi^{D}/\omega \approx 400$ μm or more.

The predicted high peak of the temperature of the injector during a cycle in the presence of deposit has numerous consequences. One is that the peak temperature is high enough for gasification of the deposit to occur [77,76], suggesting a probable removal mechanism. The cycling of T_{tip} could also cause significant thermal stress in the deposits, causing them to fracture. The temperature oscillations also complicate the modelling of the process of formation of deposits. In Sec. 2.1.2 & 2.3.1, we worked under the assumption that T_{tip} is constant during the cycle. According to Figure 8, this is a reasonable approximation only in case that the surface is fresh and no more than 5-10 μm of deposit film is accumulated – i.e. the results for $\Delta h_{tip}/\tau$ are valid only for the initial stages of the deposition process. Once enough deposit has been accumulated, the temperature peaks may result into serious acceleration of the deposition process at the tip of the injector. At the surface of a thick deposit, the boiling range will also change dramatically compared to the one in Figure 1. The analysis of this more complicated situation is left for another study.

4 Discussion

We presented a model of the fuel degradation process under engine conditions, and a model of the formation of external injector deposits. The medium in which the process of deposit formation takes place is identified as the fuel drop leaking out of the nozzle after each injection (Sec. 2.1.2). The initiator of the radical chain in the liquid fuel is identified as NO_2 produced in the combustion gases (Sec. 2.1.3), in agreement with the hypothesis of many researchers for the similar process of lubricant film degradation in the cylinder [52-56]. In addition, we identified one branching reaction by which NO contributes to the liquid phase oxidation: $RO_2\cdot + \cdot NO \rightarrow RO\cdot + \cdot NO_2$ [57,35].

The variations in the temperature and the composition of the leaked droplet are predicted. Two interesting features are found. First, as the pressure in the cylinder decreases during the power stroke, the fuel droplet reaches its boiling temperature and vaporizes, retreating simultaneously to the nozzle hole, Sec. 2.1.2. This is the probable trigger of the precipitation of deposits at the tip of the injector. Second, a cyclic accumulation regime of oxidation holds: the time between the formation and the removal of the leaked droplet is very short (few ms), insufficient for the peroxide radicals to reach their stationary concentration (15). Due to the branching reaction with NO and the slow termination rate, the overall rate of the oxidation

process is very different from the one in the classical studies of oxidation under laboratory conditions [34,35,63].

We formulate two mechanisms for the deposition of the oxidation products formed in the leaked droplet. The first one acts at the tip of the injector (Sec. 2.3.1), and involves cycles of **(i)** convective *re-suspension* (due to the injection and thermal Marangoni flow) of the deposit particles that precipitated in the previous cycle; **(ii)** *filtration* – the suspended particles filter the fuel by adsorbing the oxidized products; **(iii)** *precipitation* of the particles triggered by the boiling (perhaps following the coffee ring mechanism).

The accumulation of particles inside the nozzle channel is unlikely, as each injection will sweep them away completely. Therefore, we formulated a second mechanism for the formation of the nozzle channel deposits (Sec. 2.3.2), involving **(i)** *direct oxidation of the interface* polar deposit|fuel, with formation of polar sites at the surface, and **(ii)** *adsorption* of degradation products from the film at these polar sites.

In the absence of suitable quantitative data, the main criteria for validity of these mechanisms are the self-consistency and the agreement with the qualitative observations from the literature. The two mechanisms provide explanation of a number of known experimental facts: **(i)** the role of the distillation characteristics of the fuel for the deposition process [7] (through their direct relation to the point of boiling, Figure 1); **(ii)** the role of the injector wall temperature [50] (which controls the rate of the fuel droplet degradation); **(iii)** we obtain reasonable order of magnitude of the rates of formation (Sec. 2.3.3), and **(iv)** correct trend of the rate of formation as a function of the wall temperature (compare Figure 7 and Ref. [7]); **(v)** why certain thermally stable HC components in the fuel result in worse deposit problem (Sec. 2.3.1&2.3.2). We should add here that **(vi)** the degradation mechanism provides the correct order of magnitude of the oxygen concentration in the young deposit – each molecule in the deposit contains 1-2 oxygen atoms, which is in agreement with the high O-content found in young deposits (10-20 *w*% [5]).

The mechanisms also allow us to hypothesize why are various anti-deposit measures effective: why the additives used to fight with the tip deposits have the functionality of dispersants [24,77,73] (they interfere in the precipitation stage of the deposition); why are antioxidants added to the fuel [24] (they decelerate the autooxidation); why reducing roughness is important [8] (cf. Eq (21)). A decrease of the residual fuel that leaks out of the injector after the injection is a working strategy against deposits [8], and the new DISI injectors use designs that minimize the injector tip wetting [3]. A stepwise increase of the diameter of the hole in the end of the channel (counterbore, step hole) helps avoiding deposits [88] – this can be explained with the altered conditions of the leakage and with the hindered diffusion of the dangerous gas-phase species towards the liquid film in the narrow part of the channel (this is a sacrificial technique, as the counterbore itself suffers from serious deposit accumulation [78]). Similarly, there are designs where aluminium caps are protecting the nozzle tip from combustion gases [89,90]. Our mechanism offers a plausible explanation of why anti-deposit coatings only delay the onset of injector deposits [8] – most of the growth process occurs at the deposit|fuel interface, and once the injector surface is covered by even a very thin deposit layer, the surface chemistry of the injector itself becomes irrelevant for the process.

We present also models of some of the adverse effects the deposits have on the injector's performance and the thermal conditions at its surface. First, the nozzle channel deposits lead to plugging of the nozzle channel [8,17]. The relation between the reduction of the flow rate and the deposit thickness is approximately linear, with slope equal to $2/R_n$, Eq (27). This result allows data for the reduction to be used for the calculation of the absolute value of the deposit thickness, Sec. 3.1. To our knowledge, these data were used only for qualitative conclusions previously. Second, we investigated the effect of the injector tip deposits on the injector wall temperature, Sec. 3.2. Due to the heat insulation of the wall, the temperature of the injector

surface increases with the deposit thickness. Our analysis shows that this effect is not prominent, Figure 8-*right*. The deposits have, however, a very strong amplifying effect on the temperature oscillations during a cycle. Thus, if the temperature at the neat metal surface oscillates within a range of 4 K, a deposit of thickness 200 μm will increase this range to 80 K, Figure 8-*left*.

Due to the complexity of the system, our modelling involves by necessity a long list of approximations. Many of the relevant phenomena are modelled only roughly, and others are completely neglected. Let us give a brief summary of the main approximations, outlining meanwhile our plans for future work. The transfer of NO and NO_2 to the film is modelled crudely, using the empirical pair mixing fraction ξ [42]. In view of the complicated boundary conditions of the turbulent mass transfer process, we are pessimistic regarding the advance of a more realistic approach. The evolution of the volume of the fuel droplet is nearly neglected (we model it as a stepwise function of time); a better model would require reliable experimental leakage data. In several points of the model, the fuel is assumed to behave as a single component alkane. In particular, we neglect the detailed distillation curve and the related enrichment with less volatile components during boiling [51,22]. A model involving a mixture will lead to qualitatively new characteristics of the process, e.g., instead of point of boiling, the leaked droplet will pass through a boiling stage that would continue for few ms, during which fuel degrades. Next, we neglected completely the role of the lubricant. The tip deposits may contain 10-50% lubricant-derived ash [8,28]; lubricant elements have been found even deep inside the nozzle channel [17,28]. This ash is dispersed inside the characteristic sticky organic porous matrix (the "*oxygen skeleton*" [91]) produced by the fuel degradation and certainly plays an important role – at the very least, it reinforces the deposit, making it hard. We also neglect completely the natural polar components and the polar additives that all fuels contain; we intend to consider this question in a separate study. The role of the fuel blends is far more complicated, since these blends are usually polar components (e.g., ethanol for gasoline, esters in biodiesel) that change drastically the conditions of the liquid phase oxidation (solvent ability of the fuel, in particular). Next, once the leaked droplet boils away, we consider no details of the further evolution of the non-volatile residue. We do not analyse the removal processes, apart from the empirical $k_r h_n$ term in Eq (23). The mechanism by which the next droplet re-suspends the deposit is also not considered. It is likely that each next fuel droplet dribbling out of the nozzle dissolves some material deposited by the previous droplet, which we neglect, i.e. we assume that the deposition is irreversible. With regard to the nozzle channel deposits, the crudest approximation we use is for the transport of mass and heat from the tip droplet to the nozzle channel (cf. Ref. [1]). The oxidation mechanism is simplified; for example, at these levels, the nitrogen oxides in the quench layer can participate in other interesting reactions [35] – unfortunately, we do not dispose of the values of the respective rate parameters. Additionally, in order to consider real fuels, we need to add in our model the possibility for intramolecular propagation, alkene and alkylarene oxidation, bulk formation of polyfunctional degradation products and mechanisms of their adsorption and polymerization. Metal catalysis is probably also a factor [8].

With regard to the effects of the deposits on the injector performance, many possibilities to make our models in Sec. 3 more realistic exist. For example, one can consider how the turbulent shear affects the nozzle channel deposits, which can result in a primitive model of the k_r parameter in Eq (23). Another question of importance is, how would the evaporating fuel film affect the heat transfer through the wall? The fuel wets the deposit, changing its heat transfer parameters, and it also consumes heat during evaporation.

Another interesting problem is, how the engine operating conditions affect the deposition process? Our SRM engine model allows the pressure profile, the profile of the heat flux to the wall and respectively – the wall temperature to be simulated at various engine loads, and their

effect on the deposition rate can be followed. This is not straightforward to do, however, as one must deal with the dependence of the ξ-parameter and the leaked droplet volume on the speed of the engine. In the same line of thoughts, it is known that the oxidation processes, the adsorption of gases etc. continue long after the deposit is formed, even after the engine is switched off (e.g. *sec. 5.2* in Ref. [73]). It is also known that the trapped residue contributes to the deposition process [59] – currently, our residue model is simplified (cf. S1).

The model we developed can be transferred to several interesting similar questions. For example, it has been found that liquid phase oxidation occurs in the spray droplets at a rate that is several orders of magnitude higher than the oxidation of bulk fuel [92], probably again under the action of NO_x. It seems possible that a solid residue can be left after the spray droplets boil, which can contribute to soot formation and HC emissions. Our model can be used to investigate this problem with only minor modifications. The degradation of the impinged fuel film at the piston [51,42] should also follow a similar mechanism.

Finally, let us mention that we considered neither the formation of the seat and needle ball deposits nor their effect on the HC emissions. The reason is that data for these deposits is scarce [8]. We believe that the seat and ball deposits are responsible, at least in part, for these HC emissions. The obvious effect from them is worse sealing – roughly, if the seal has thickness h_s, the presence of the sparsely distributed deposits observed in Ref. [8] of certain thickness h_{seat} would result in the increase of the seal thickness to $\sim h_s + 2h_{seat}$, leading to an increased leakage rate (proportionally to $(h_s + 2h_{seat})^3$ [93]). Indeed, increased leakage has been observed recently with fouled injectors [9]. Leakage is a major contributor to the HC emissions. Its rate is ~1 g per kg fuel [46,3], and at least ¼ of the leaked fuel will be released directly in the exhaust. For the data in Table 2, this corresponds to 0.4 g HC emissions per 23.8+1.6 = 25.4 kg mixture, or 16 *w*ppm, which is significant (typically, HC emissions are of the order of 50 *w*ppm). The increase of the leakage with few percent due to injector deposits will contribute to the HC emissions an amount similar to the observed one. In diesel engines, the impinged fuel film due to the adverse effect of the deposit on the spray characteristics is another source of HC emissions.

Acknowledgements. The authors would like to acknowledge the funding and technical support from BP through the BP International Centre for Advanced Materials (BP-ICAM) which made this research possible. This research is partly funded by the National Research Foundation (NRF), Prime Minister's Office, Singapore under its Campus for Research Excellence and Technological Enterprise (CREATE) programme.

References

The publication contains supplementary materials: S1. Engine parameters and cylinder conditions. **S2.** Rate parameters of the liquid phase oxidation. **S3.** Gas transfer to the liquid film. **S4.** Nozzle channel deposits: relationship between flow reduction and deposit thickness, and processing of the experimental data. **S5.** The multilayer heat transfer problem. **S6.** List of symbols and abbreviations.

1. Y.C. Wang. Study of deposit formation inside diesel injectors nozzles. PhD Thesis, Massachusetts Institute of Technology (2012).
2. W.E. Eagle, M.P.B. Musculus. Cinema-stereo imaging of fuel dribble after the end of injection in an optical heavy-duty diesel engine. *Thiesel Conference Proceedings*, 2014, SAND2014-15805C, OSTI 1314615.

3. T. Pauer, H. Yilmaz, J. Zumbrägel, E. Schünemann. New generation Bosch gasoline direct-injection systems. MTZ Worldw. 78 (2017) 16-23, doi.org/10.1007/s38313-017-0053-6.
4. S. Moon, W. Huang, Z. Li, J. Wang. End-of-injection fuel dribble of multi-hole diesel injector: Comprehensive investigation of phenomenon and discussion on control strategy. *Applied Energy* **179** (2016) 7–16.
5. A.M. Liaquat, H.H. Masjuki, M.A. Kalam, M.A. Fazal, A.F. Khan, H. Fayaz, M. Varman. Impact of palm biodiesel blend on injector deposit formation. *Applied Energy* **111** (2013) 882–893.
6. R. Venkataraman, S. Eser. Characterization of deposits formed on diesel injectors in field test and from thermal oxidative degradation of n-hexadecane in a laboratory reactor. *Chem. Cent. J.* **2** (2008) 25.
7. M. Kinoshita, A. Saito, S. Matsushita, H. Shibata, Y. Niwa. Study of deposit formation mechanism on gasoline injection nozzle. *JSAE Review* **19** (1998) 351–371.
8. H. Xu, C. Wang, X. Ma, A. K. Sarangi, A. Weall, J. Krueger-Venus. Fuel injector deposits in direct-injection spark-ignition engines. *Progress Energy Combust. Sci.* **50** (2015) 63–80.
9. Y. Wen, Y. Wang, C. Fu, W. Deng, Z. Zhan, Y. Tang, X. Li, H. Ding, S. Shuai. The impact of injector deposits on spray and particulate emission of advanced gasoline direct injection vehicle. *SAE* 2016-01-2284.
10. I. Celik, O. Aydin. Effects of B100 biodiesel on injector and pump piston. *Tribol. T.* **54** (2011) 424–431.
11. B. Wang, Y. Jiang, P. Hutchins, T. Badawy, H. Xu, X. Zhang, A. Rack, P. Tafforeau. Numerical analysis of deposit effect on nozzle flow and spray characteristics of GDI injectors. *Applied Energy* **204** (2017) 1215-1224.
12. C. Wang, H. Xu, J.M. Herreros, J. Wang, R. Cracknell. Impact of fuel and injection system on particle emissions from a GDI engine. *Applied Energy* **132** (2014) 178-191.
13. J. Tang, S. Pischinger, M. Lamping, T. Körfer, M. Tatur, D. Tomazic. Coking phenomena in nozzle orifices of di-diesel engines. *SAE* 2009-01-0837.
14. J. Reid, S. Cook, J. Barker. Internal injector deposits from sodium sources. *SAE Int. J. Fuels Lubr.* **7** (2014), *SAE* 2014-01-1388.
15. J. Barker, J. Reid, C. Snape, D. Scurr, W. Meredith. Spectroscopic studies of internal injector deposits (IDID) resulting from the use of non-commercial low molecular weight polyisobutylenesuccinimide (PIBSI). *SAE Int. J. Fuels Lubr.* **7** (2014), *SAE* 2014-01-2720.
16. P.S.V. Bacho, J.K. Sofianek, J.M. Galante-Fox, C.J. McMahon. Engine test for accelerated fuel deposit formation on injectors used in gasoline direct injection engines. *SAE technical paper* 2009-01-1495.
17. A.A. Aradi, B. Imoehl, N.L. Avery, P.P. Wells, R.W. Grosser. The effect of fuel composition and engine operating parameters on injector deposits in a high-pressure direct injection gasoline (DIG) research engine. *SAE* 1999-01-3690.
18. S.S. Cheng. A micrographic study of deposit formation processes in a combustion chamber. *SAE* (1996) 962008.
19. G. Lepperhoff, M. Houben. Mechanisms of deposit formation in internal combustion engines and heat exchangers. *SAE* 931032.
20. B.L. Papke, C.B. Charles. Development of a Laboratory Test to Simulate Piston Deposit Formation in the ASTM Sequence IIIG Engine Test. STLE, May 2012 (presentation).
21. P.W. Guthrie. A review of fuel, intake and combustion system deposit issues relevant to 4-stroke gasoline direct fuel injection engines. *SAE Paper* 2001-01-1202.
22. Y. bin Mohamed Arifin. Diesel and bio-diesel fuel deposits on a hot wall surface. PhD thesis, Gunma University, Japan (2009).
23. G.T. Kalghatgi. Combustion chamber deposits in spark-ignition engines: a literature review. *SAE* 952443.

24. V.M. Kapustin. Petroleum and alternative fuels with additives and dopants. KolosS, Moscow (2008). In Russian; p. 35–39.
25. C. O'Brien. Formation mechanism of combustion chamber deposits. PhD Thesis, Massachusetts Institute of Technology (2001).
26. J. Barker, J. Reid. Injector and fuel system deposits. Paper from 10th International Colloquium Fuels Conventional and Future Energy for automobiles, 2015, Technische Akademie Esslingen in Stuttgart/Ostfildern.
27. A. Tanaka, K. Yamada, T. Omori, S. Bunne, K. Hosokawa. Inner diesel injector deposit formation mechanism. *SAE* 2013-01-2661.
28. K. Dearn, J. Xu, H. Ding, H. Xu, A. Weall, P. Kirkby, B. Cooper, I. Edington, J. Krueger-Venus. An investigation into the characteristics of DISI injector deposits using advanced analytical methods. *SAE* 2014-01-2722.
29. S. Taniguchi, K. Yoshida, Y. Tsukasaki. Feasibility study of ethanol applications to a direct injection gasoline engine journal. *SAE* 2007-01-2037.
30. J. Barker, P. Richards, C. Snape, W. Meredith. A Novel Technique for Investigating the Nature and Origins of Deposits Formed in High Pressure Fuel Injection Equipment. *SAE Int. J. Fuels Lubr.* **2** (2009) 38–44.
31. C. Kim, S. Tseregounis, B. Scruggs. Deposit Formation on a Metal Surface in Oxidized Gasolines. *SAE* 872112.
32. A.B. Amara, A. Nicolle, M. Alves-Fortunato, N. Jeuland. Toward predictive modeling of petroleum and biodiesel fuel stability: kinetics of methyl oleate/n-dodecane autooxidation. *Energy Fuels* **27** (2013) 6125–6133.
33. V.R. Katta, E.G. Jones, W.M. Roquemore. Modeling of deposition process in liquid fuels. *Combust. Sci. Tech.* **139** (1998) 75–111.
34. C.H. Bamford, C.F.H. Tipper (editors). Comprehensive Chemical Kinetics. Liquid-Phase Oxidation. Elsevier: Amsterdam, Netherlands, 1980.
35. E.T. Denisov, I.B. Afanas'ev. Oxidation and antioxidants in organic chemistry and biology. CRC Taylor & Francis, 2005.
36. CMCL Innovations. SRM Engine Suite, version 8.9, 2016, http://www.cmclinnovations.com/srm/.
37. S.B. Pope. PDF methods for turbulent reactive flows. *Prog. Energy Combust. Sci.* **11** (1985) 119–192.
38. S. Mosbach, M.S. Celnik, A. Raj, M. Kraft, H.R. Zhang, S. Kubo, K.O. Kim. Towards a detailed soot model for internal combustion engines. *Combust. Flame* **156** (2009) 1156–1165.
39. S. Subramaniam, S. B. Pope. A Mixing Model for Turbulent Reactive Flows based on Euclidean Minimum Spanning Trees. *Combust. Flame* **115** (1998) 487–514.
40. H. Su, A. Vikhansky, S. Mosbach, M. Kraft, A. Bhave, K. Kim, T. Kobayashi, F. Mauss. A computational study of an HCCI engine with direct injection during gas exchange. *Combust. Flame* **147** (2006) 118–132.
41. J. Etheridge, S. Mosbach, M. Kraft, H. Wu, N. Collings. Modelling soot formation in a DISI engine. *Proc. Combust. Inst.* **33** (2011) 3159-3167.
42. B. Wang, S. Mosbach, S. Schmutzhard, S. Shuai, Y. Huang, M. Kraft. Modelling soot formation from wall films in a gasoline direct injection engine using a detailed population balance model. *Appl. Energy* **163** (2016) 154–166.
43. J. Etheridge, S. Mosbach, M. Kraft, H. Wu, N. Collings. Modelling cycle to cycle variations in an SI engine with detailed chemical kinetics. *Combust. Flame* **158** (2011) 179–188.

44. S. Mosbach, H. Su, M. Kraft, A. Bhave, F. Mauss, Z. Wang, J.-X. Wang. Dual injection homogeneous charge compression ignition engine simulation using a stochastic reactor model. *Int. J. Engine Research* **8** (2007) 41–50.
45. L. Zigan, J.-M. Shi, I. Krotow, I. Schmitz, M. Wensing, A. Leipertz. Fuel property and fuel temperature effects on internal nozzle flow, atomization and cyclic spray fluctuations of a direct injection spark ignition-injector. *Int. Journal of Engine Research* **14** (2013) 543-556.
46. W. Ethan Eagle, M.P.B. Musculus. Image-based correlation of engine operating parameters with occurrence and duration. SAND2015-3098C.
47. R. Pearson, M. Gold, S. Filip, J. Turner, V. Stetsyuk, C. Crua, J. Gilchrist, S. Heutz, M. Ryan, P. Howard. Transient effects of fuel sprays on the surface wetting of diesel fuel injectors. Presentation at the SAE International Powertrains, Fuels & Lubricants Meeting, Baltimore, Maryland, USA, 24-26 October 2016.
48. E.R. Smith. Boiling points of n-heptane and 2,2,4-trimethylpentane over the range 100- to 1,500-millimeter pressure. *J. Research Nat. Bureau Standards* **24** (1940) 229-234.
49. R.I. Slavchov, J.K. Novev, S. Mosbach, M. Kraft. Vapour pressure and vaporization heat of molecules that associate in the gas phase. *Ind. Eng. Chem. Res.* (2018), just accepted, DOI 10.1021/acs.iecr.7b04241.
50. A.A. Aradi, W.J. Colucci, H.M. Scull, M.J. Openshaw. A study of fuel additives for direct injection gasoline (DIG) injector deposit control. *SAE* 2000-01-2020.
51. C. Baumgarten. Mixture formation in internal combustion engines. Springer-Verlag Berlin/Heidelberg (2006).
52. E. Dimitroff, J.V. Moffitt, R.D. Quillian. *Trans. ASME* **91** (1969) 406–410.
53. J.B. Hanson, S.W. Harris, C.T. West. *SAE* 881581.
54. R.R. Kuhn. *ACS Preprints Div. Petrol Chem.* **18** (1973) 697–698.
55. M.D. Johnson, S. Korcek. *Lubrication Sci.* N**3** (1991) 95–101.
56. M.D. Johnson, S. Korcek, M.J. Rokosz. *Lubrication Sci.* N6 (1994) 247–251.
57. T.J. Wallington, P. Dagaut, M.J. Kurylo. Ultraviolet absorption cross sections and reaction kinetics and mechnisms for peroxy radicals in the gas phase. *Chem. Rev.* **92** (1992) 667–710.
58. J. Warnatz, U. Maas, R.W. Dibble. Combustion, 4th ed. Springer, 2006. Sec. 21.2.
59. J.B. Heywood. Internal combustion engine fundamentals. McGraw-Hill, Inc. (1988).
60. L.R. Rudnick (editor). Lubricant additives: chemistry and applications, 2nd ed. CRC Press (2009).
61. K.S. Suslick, M.M. Mdleleni, J.T. Ries. *J. Am. Chem. Soc.* **119** (1997) 9303-9304.
62. H.E. Merritt. Hydraulic control systems. Wiley & Sons, New York (1967).
63. F.R. Mayo, T. Mill. Gum and deposit formation in diesel fuels. Final report for the US Army Research Office (1988).
64. S. Zabarnick. Chemical kinetic modelling of jet fuel autooxidation and antioxidant chemisty. *Indust. & Engin. Chem. Research* **32** (1993) 1012−1017.
65. T. Mill, G. Montrosi. The liquid-phase oxidation of 2,4-dimethylpentane. *Int. J. Chem. Kin.* **5** (1973) 119–136.
66. D.E. Van Sickle. Oxidation of 2,4,6-trimethylheptane. *J. Org. Chem.* **37** (1972) 755–760.
67. D.E. Van Sickle, T. Mill, F.R. Mayo, H. Richardson, C.W. Gould. Intramolecular propagation in the oxidation of n-alkanes. Autooxidation of n-pentane and n-octane. *J. Org. Chem.* **38** (1973) 4435–4440.
68. N.M. Emanuel', D.G. Knorre. A course in chemical kinetics, 4th ed. Vysshaya shkola, Moscow, 1984.
69. J.K. Novev, N. Panchev, R.I. Slavchov. Evaporating foam films of pure liquid stabilized via the thermal Marangoni effect. *Chem. Eng. Sci.* **171** (2017) 520-533.

70. S.N. Mendiara, A. Segadahl, L.J. Perissinotti. An electron paramagnetic resonance study of nitrogen dioxide dissolved in water, carbon tetrachloride and some organic compounds. *Appl. Magn. Reson.* **20** (2001) 275–287.
71. S.N. Mendiara, L.J. Perissinotti. Dissociation equilibrium of dinitrogen tetroxide in organic solvents: an electron paramagnetic resonance measurement. *Appl. Magn. Reson.* **25** (2003) 323–346.
72. H. Hu, R.G. Larson. Marangoni effect reverses coffee-ring depositions. *J. Phys. Chem. B* **110** (2006) 7090–7094.
73. S.P. Srivastava, J. Hancsóc. Fuel and fuel additives. Wiley, Hoboken, New Jersey (2014).
74. S.P. Heneghan, S. Zabarnick. Oxidation of jet fuels and the formation of deposits. *Fuel* **73** (1994) 35–43.
75. R.N. Wenzel. Resistance of solid surfaces to wetting by water. *Ind. Eng. Chem.* **28** (1936) 988–994.
76. H.H. Abou el Naga, A.E.M. Salem. Base oils thermooxidation. *Lubr. Eng.* **42** (1986) 210–217.
77. E.R. Magaril, R.Z. Magaril. Engine fuels. Moscow (2008), in Russian.
78. C. Jiang, H. Xu, D. Srivastava, X. Ma, K. Dearn, R. Cracknell, J. Krueger-Venus. Effect of fuel injector deposit on spray characteristics, gaseous emissions and particulate matter in a gasoline direct injection engine. *Applied energy* **203** (2017) 390-402.
79. T.P. Vishnyakova, I.A. Golubeva, I.F. Krilov, O.P. Likov. Stabilizers and modificators of petroleum distillate fuels. Khimiya (1990), in Russian.
80. R. Lindgren, M. Skogsberg, H. Sandquist, I. Denbratt. The influence of injector deposits on mixture formation in a DISC SI engine. *JSAE* 20030110.
81. S. Henkel, Y. Hardalupas, A. Taylor, C. Conifer, R. Cracknell, T.K. Goh, P.-B. Reinicke, M. Sens, M. Riess, Injector fouling and its impact on engine emissions and spray characteristics in gasoline direct injection engines. SAE 10.4271/2017-01-0808.
82. J. Storey, S. Lewis, M. Moses-DeBusk, R. Connatser, J. Lee, T. Tzanetakis, K. Cho, M. Lorey, M. Sellnau. Characterization of hydrocarbon emissions from gasoline direct-injection compression ignition engine operating on a higher reactivity gasoline fuel. SAE 10.4271/2017-01-0747.
83. C.F. Colebrook. Turbulent flow in pipes, with particular reference to the transition region between smooth and rough pipe laws. *J. Institution Civil Engineers* **11** (1939) 133–156.
84. A.H. Shapiro, R. Siege., and S.J. Kline. Friction factor in the laminar entry of a smooth tube. Proc. 2nd Us Natl. Congr. Appl. Mech. (1954) 733-741.
85. X.L.J. Seykens, L.M.T. Somers, R.S.G. Baert. Modelling of common rail fuel injection system and influence of fluid properties on injection process. *Proceedings of VAFSEP2004, July 2004, Dublin*.
86. E.R. Magaril, R.Z. Magaril, V.G. Bamburov. Specific features of combustion in gasoline-driven internal combustion engines. *Combust. Explo. Shock Waves* **50** (2014) 75.
87. J. Crank. The Mathematics of Diffusion. Oxford Science Publications (1979).
88. P.G. Aleiferis, J. Serras-Pereira, A. Augoye, T.J. Davies, R.F. Cracknell, D. Richardson. Effect of fuel temperature on in-nozzle cavitation and spray formation of liquid hydrocarbons and alcohols from a real size optical injector for direct-injection spark-ignition engines. *Int. J. Heat Mass Transfer* **53** (2010) 4588–4606.
89. B.Y. Tanaguchi, R.J. Peyla, G.M. Parsons, S.K. Hoekman, D.A. Voss. Injector deposits – the tip of intake system deposit problems. *SAE* 861534.
90. F. Caracciolo, R.F. Stebar. An engine dynamometer test for evaluation port fuel injector plugging. *SAE* 872111.
91. G.T. Kalghatgi. Deposits in gasoline engines – a literature review. *SAE* 902105.

92. G.S. Shimonaev. On the catalytic action of the metal on the oxidation of fuels and oils. *Khimiya i tekhnologiya topliv i masel* (1978) 47–49. In Russian.
93. R. Stone. Introduction to internal combustion engines, 2nd ed. MacMillan Press (1992), p. 212.

An adsorption-precipitation model for the formation of injector external deposits in internal combustion engines

Supplementary information

Radomir I. Slavchov[*,1], Sebastian Mosbach[1], Markus Kraft[1,2], Richard Pearson[3], Sorin Filip[3]*

[1]*Department of Chemical Engineering and Biotechnology, University of Cambridge, UK*
[2] *School of Chemical and Biomedical Engineering, Nanyang Technological University, Singapore*
[3]*BP International Ltd, Pangbourne, UK*
* E-mail: ris26@cam.ac.uk

S1. Engine parameters and cylinder conditions

In this supplement, we are giving additional details of the engine model used for the SRM simulations. All the characteristics that are not provided here or in the text are unchanged compared to the default DISI case in SRM Engine Suite and are described in Refs. [43,42] (including the parameters of the Euclidean minimum spanning tree model of the mixing, the model for the heat transfer between the stochastic particles, the variation of Woschni's correlation used for the charge-wall heat transfer, the spark characteristics, friction model and others). In addition to the data in Table 1, the following two basic characteristics of the cylinder have been set to those of the real test engine we model: manifold intake pressure = 70 kPa; exhaust port pressure = 126 kPa. All simulations used 240 bulk cylinder stochastic particles and 20 quench layer stochastic particles.

The injection event has little effect on the outcome of the simulation due to the early injection strategy utilized by the real engine we are modelling. In the real engine, the injection event occurs during the intake stroke, at -311 CAD, while inlet valve is still opened. Presumably, at the time of the inlet valve closure, the fuel is already atomized completely. Under the early injection strategy, the precise timing of the injection is unimportant for most engine characteristics. For simplicity, we simulate only the closed-volume part of the cycle, i.e. the compression and power strokes, and set the injection event between -180 and -150 CAD, as well as set the characteristic turbulent mixing time at a relatively small value (1 ms). This guarantees that the mixture is well-mixed long before TDC, without significant compositional stratification, and ensures independence of all relevant simulated quantities on the injection characteristics. The inlet valve closure and exhaust valve opening are assumed to occur at -180 and +180 CAD, respectively.

An important feature of the test engine is that, as most gasoline engines, it operates with a substantial amount of residual combustion gas in the charge mass. The amount of the residual gas was calculated by solving an integral mass balance, using the known characteristics of the real engine, namely, the air & fuel consumption of the engine; the manifold intake pressure and temperature (37°C – which is assumed to be the air temperature before mixing with the hot exhaust); the exhaust manifold pressure and temperature (assumed equal to those of the trapped residue before mixing it with the cold air). When writing the mass balance, we also took into account that the evaporated fuel contributes to the pressure of the cylinder charge. The exhaust in our simulation has 5 components: N_2, H_2O, CO_2, CO and NO – these were the components of highest concentration in the exhaust obtained in a preliminary simulation performed without

trapped residue being accounted for. These data allowed us to calculate the composition of the cylinder charge at the start of the simulation, given in **Table S1**.

Table S1: Composition of the initial charge.

component	*w*%
N_2	76.656
O_2	21.603
CO_2	1.121
H_2O	0.576
CO	0.038
NO	0.006

An important consequence of the presence of trapped residual gas is the increased temperature of the charge upon inlet valve closure. It was calculated approximately, by assuming that the mixing between the fresh charge and the trapped residue is adiabatic – this assumption results in 82.2°C. Many results of the simulation (pressure profile, deposition rates) were found to have a non-negligible dependence on both the residue components amount and the initial temperature.

We will now present some of the simulation results of secondary importance. In **Figure S1**, the simulated values of CAD_0 and CAD_b are shown as function of the wall temperature. As seen, they follow closely the average dependence of the boiling temperature vs. CAD (the small variations are due to the stochastic nature of our simulations). The possible regimes of accumulation of the leaked fuel are delineated with grey dash lines (cf. Sec. 2.1.2).

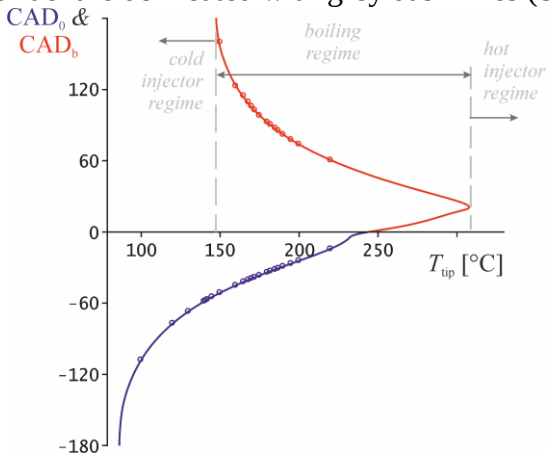

Figure S1: Points of boiling and precipitation as function of the injector tip surface temperature. The points are the results of full simulations; the curve is the rotated boiling temperature curve in Figure 1-*right* as obtained from the base case simulation (T_{tip} = 160°C).

In **Figure S2**, the evolution of the oxygen concentration in the quench layer is illustrated. The quench layer is at temperature fixed to T_{tip} (160°C for the example). The oxygen has little time to escape during the power stroke (~5 ms), i.e. the molar part of O_2 in the quench layer does not change significantly. However, cylinder pressure increases and compresses the quench layer, leading to significant increase of $[O_2]^G$ there, Figure S2-*left*. In Figure S2-*right*, we calculate the reduction of the amount of O_2 in the quench layer during a cycle in comparison with the theoretical O_2 concentration *unperturbed* by diffusion, $[O_2]^G_{unpert.}$, given by $x_{O_2}(CAD = -180°)\times p/RT_{tip}$, where $x_{O_2}(CAD = -180°)$ is the initial value of the molar part of the oxygen. During the compression stroke, there is little change of the quench layer composition as quench layer and cylinder charge have similar fractions of O_2. During the power stroke, the oxygen in the cylinder is depleted (Figure S2-*left*), and diffusion from the quench layer to the

bulk starts. For the few milliseconds before the exhaust valve opens, about 6% of the O_2 present the quench layer is transported to the cylinder. As the time for a stroke is 10.6 ms, one can estimate that the time needed for half of the oxygen to leave the quench layer is of the order of 100 ms (which is obviously related to the chosen value of the empirical parameter ξ, cf. Sec. 2.1.3). We assume that, during the exhaust and the intake stroke where gas velocity in the bulk is very large, the quench layer is substituted with a fresh gas. Probably, this is not completely fulfilled in reality.

Let us mention that the precise concentration of the oxygen in the quench layer or in the film is irrelevant for the rate of deposition (which is valid also for most classical cases of liquid phase oxidation rates [34,35,63]). The concentration of O_2 in the quench layer may have relevance only under exceptional conditions, such as extremely low $[O_2]$ which can cause depletion effects, or very high $[O_2]$ which may result into rate of the reaction $RH + O_2 \rightarrow R\cdot + HO_2\cdot$ high enough to contribute to the initiation rate. For the considered study case, the exact value of $[O_2]$ is of little importance.

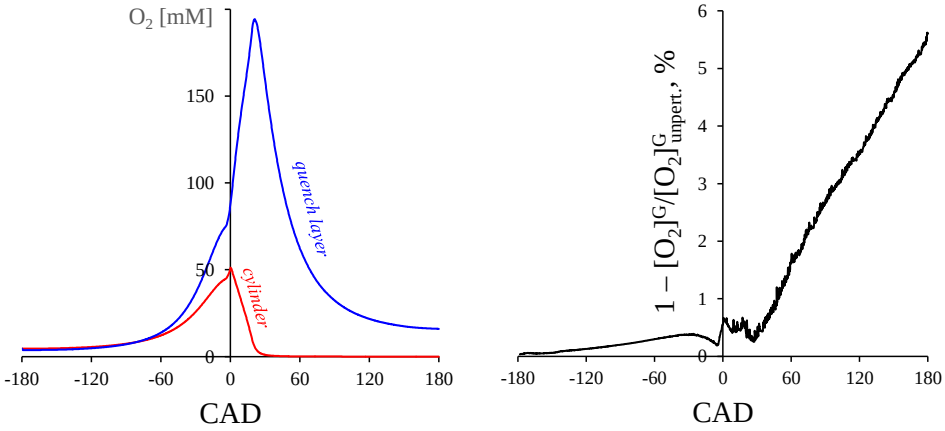

Figure S2-*left*: Concentration of O_2 in the cylinder and in the quench layer as a function of CAD. *Right*: reduction of the fraction of O_2 in the quench layer during a cycle due to the transport toward the bulk. About 6% of the oxygen escapes the quench layer for the time of the power stroke.

In **Figure S3**, the evolution of three major N-containing components (NO, NO_2 and HNO_2) of the quench layer is illustrated at several values of T_{tip}. The concentration of these species decrease with T_{tip} due to the ideal gas law (concentration $\propto 1/T_{tip}$). Only at high wall temperatures (above 190°C), the concentrations of NO_2 and HNO_2 increase, due to the change of the rate of the involved reactions producing and consuming them [58].

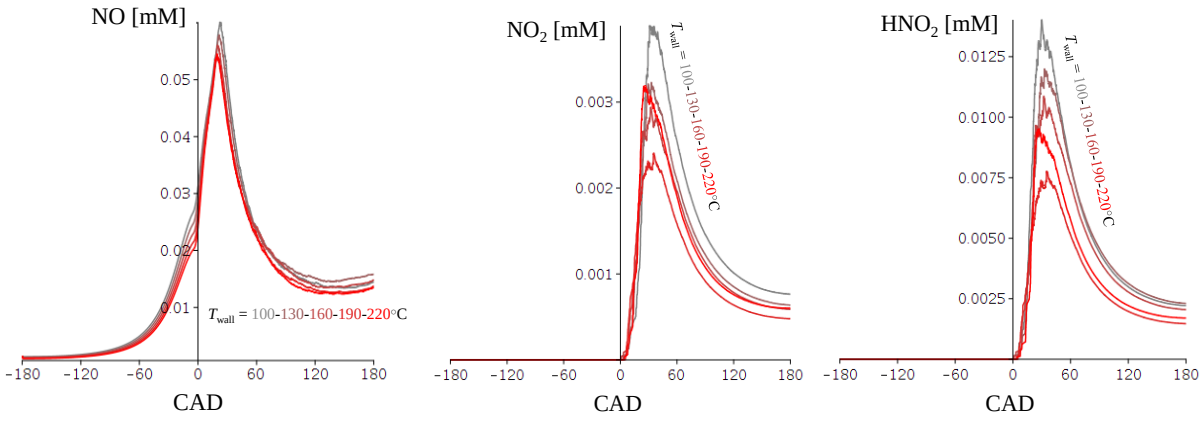

Figure S3: Concentration of NO, NO_2 and HNO_2 in the quench layer at several values of T_{tip}.

S2. Rate parameters of the liquid phase oxidation

All Arrhenius rate parameters used in this work are summarized in Table S2.

Table S2: Bulk phase oxidation – rate parameters (per active site).

Reaction	Rate parameters	References
Radical oxidation		
$R_2CH\cdot + O_2 \rightarrow R_2CHO_2\cdot$, alkane phase, 298 K	$k_o = 1.7\times10^9$ 1/sM, $E_o \approx 0$	[a] [35/p.67, table 2.4]
$R_3C\cdot + O_2 \rightarrow R_3CO_2\cdot$, cyclohexane phase, 300 K	$k_o = 4.9\times10^9$ 1/sM, $E_o \approx 0$	[35/p.67, table 2.4]
$RO_2\cdot$ propagation		
$RO_2\cdot + R_3CH \rightarrow RO_2H + R_3C\cdot$	$k_{a0} = 1.58\times10^9$ 1/sM, $E_a = 66.7$ kJ/mol	[34/p.34]
$RO_2\cdot + R_2CH_2 \rightarrow RO_2H + R_2CH\cdot$	$k_{a0} = 10^9$ 1/sM, $E_a = 69.9$-72.8 kJ/mol	[34/p.34]
RO· propagation		
$R_3CO\cdot + R_3CH \rightarrow R_3COH + R_3C\cdot$	$k_{aOH0} = 2.51\times10^9$ 1/sM, $E_{aOH} = 22.8$ kJ/mol	[34/p.51]
$R_3CO\cdot + R_2CH_2 \rightarrow R_3COH + R_2CH\cdot$	$k_{aOH0} = 1.58\times10^9$ 1/sM, $E_{aOH} = 25.9$ kJ/mol	[34/p.51]
[b] **$k_a/(2k_t)^{1/2}$**		
R_3CH	$[k_a/(2k_t)^{1/2}]_0 = 5900$ $1/s^{1/2}M^{1/2}$, $E = 50.6$ kJ/mol	[35/p.60]
R_2CH_2	$[k_a/(2k_t)^{1/2}]_0 =$ $=4.7\times10^5$ $1/s^{1/2}M^{1/2}$, $E = 66.9$ kJ/mol	[67]
RO· formation		
$2R_3CO_2\cdot \rightarrow 2R_3CO\cdot + O_2$	$a = 0.17$	[65]
$2R_2CHO_2\cdot \rightarrow 2R_2CHO\cdot + O_2$	$a = 0.5$	[67]
NO_2 initiation		
R_3CH	$k_{i0} = 5.9\times10^9$ 1/sM, $E_i = 73.6$ kJ/mol	[35/p.141, table 3.10]
R_2CH_2	$k_{i0} = 1.2\times10^{10}$ 1/sM, $E_i = 86.6$ kJ/mol	[35/p.141, table 3.10]
O_2 initiation		
R_3CH	$k_{i0} = 1.5\times10^{12}$ 1/sM, $E_i = 159.0$ kJ/mol	[35/p.169, table 4.1]
R_2CH_2	$k_{i0} = 7.94\times10^{12}$ 1/sM, $E_i = 167.4$ kJ/mol	[35/p.169, table 4.1]
[c] **NO branching**		
$RO_2\cdot + \cdot NO \rightarrow RO\cdot + \cdot NO_2$	$k_{NO} = 5\times10^9$ 1/sM	[57]

[a] Average value for cyclohexane, hexadecane & heptadecane.
[b] The values of the ratio $k_a/(2k_t)^{1/2}$ are more reliable than those for k_a or k_t alone; we used this ratio and the value of k_p to calculate k_t, but most probably the k_p values are inaccurate.
[c] Average for several alkanes in the gas phase in the considered temperature range; the temperature dependence is neglected.

Let us mention here one approximation involved in the surface oxidation mechanism proposed: that we did not consider the surface-bulk radical equilibration. This reaction is analogous to the bulk $R_1\cdot + R_2H \leftrightarrow R_1H + R_2\cdot$ process mentioned in Ref. [68]. It reads:

$$\mathrm{s}\cdot + \mathrm{RH} \underset{k^{\mathrm{S}}_{\mathrm{iR}\cdot}}{\overset{k^{\mathrm{S}}_{\mathrm{aRH}}}{\rightleftharpoons}} \mathrm{sH} + \mathrm{R}\cdot, \quad v^{\mathrm{S}}_{\mathrm{eq}} = k^{\mathrm{S}}_{\mathrm{aRH}}[\mathrm{s}\cdot][\mathrm{RH}] - k^{\mathrm{S}}_{\mathrm{iR}\cdot}[\mathrm{sH}][\mathrm{R}\cdot]. \tag{33}$$

Unlike the respective bulk-bulk equilibration, the result from the above reaction is non-trivial even for one-component fuel. Unfortunately, the equilibration parameters are hard to estimate due to the absence of data for the respective bulk ones. Therefore, we assumed that the process is of very slow rate and does not contribute to the outcome of the oxidation. As an example of the possible outcome of the process, let us consider another limiting case – the one in which the process (33) is very fast, and in which the forward and the reverse rate constants are equal to each other. This leads to the simple relation $[\mathrm{s}\cdot]/[\mathrm{sH}] = [\mathrm{R}\cdot]/[\mathrm{RH}]$.

Let us briefly consider also the approximation that each surface rate constant $k^{\mathrm{S}}_{\mathrm{x}}$ has value close to the one of the analogous bulk process k_{x}. This assumption involves two questions: what is the relation between the activation energies E and the preexponential factors k_0 in the rate constants of the surface and the bulk process. The activation energy is indeed a function of the state of the bonds involved in the reactions and their closest environment, which is not dramatically different in the fuel bulk and at the deposit|fuel interface. The main difference is the presence of increased number of O-containing functional groups in the polar deposit. These functional groups can activate the nearby C-H bonds [35], especially in the case of secondary C-H bond at the same carbon at which the polar group is attached, i.e. -CH(O_xH)-, but also with first neighbours, i.e. >CHC(O_xH)< .

With regard to the preexponential factor, a first argument for similar order of magnitude of the values of $k^{\mathrm{S}}_{\mathrm{x}0}$ and $k_{\mathrm{x}0}$ is their equivalent dimensions. A more elaborate argument can be obtained from the basic theory of these preexponential factors. We will limit ourselves with a comparison between the surface reaction sH + A, where A is assumed to be in gas phase, and RH + A in the bulk of a gas. The number ν_{A} of hits of molecules A to the wall is given by the Maxwell-Hertz-Knudsen flux – within a numerical factor, it is valid that

$$\nu_{\mathrm{A}} \sim N_{\mathrm{A}}\sqrt{\frac{RT}{M_{\mathrm{A}}}}[\mathrm{A}]. \tag{34}$$

The respective rate v_{A} of the reaction between sH and A (in units [m^2/s mol]) is [68]:

$$v_{\mathrm{A}} \sim N_{\mathrm{A}}\sqrt{\frac{RT}{M_{\mathrm{A}}}}[\mathrm{A}]\sigma_{\mathrm{HA}}[\mathrm{sH}]\mathrm{e}^{-E/RT}, \tag{35}$$

where exp(–E/RT) occurs due to the potential barrier E; σ_{HA} is the cross-section of the reaction (treated as area per sH site which, if hit by A, can result in reaction). The dimensionless quantity $\sigma_{\mathrm{HA}}[\mathrm{sH}]N_{\mathrm{A}}$ is the fraction of area available for reaction. Thus, the preexponential factor of the surface reaction is:

$$k^{\mathrm{S}}_{\mathrm{x}0} \sim N_{\mathrm{A}}\sqrt{\frac{RT}{M_{\mathrm{A}}}}\sigma_{\mathrm{HA}}. \tag{36}$$

The respective bulk quantity for the process RH + A → … is given by [68]:

$$k_{\mathrm{x}0} \sim N_{\mathrm{A}}\sqrt{\frac{RT\left(M_{\mathrm{RH}}+M_{\mathrm{A}}\right)}{M_{\mathrm{RH}}M_{\mathrm{A}}}}\sigma_{\mathrm{HA}}. \tag{37}$$

Thus, the ratio between the preexponential factors for the considered reaction, as it follows from Eqs (36)&(37), under the assumption that σ_{HA} of the reaction does not change in case that the reactive C-H bond is bound to the surface, is the following one:

$$\frac{k_{x0}}{k_{x0}^{S}} \sim \sqrt{1+\frac{M_{RH}}{M_{A}}}\,. \qquad (38)$$

As the molar masses of RH and A are not too different, the bulk and the surface preexponential factors are expected to be of similar order of magnitude. Similar formula can be devised using the basic theory of liquid phase reactions, but with diffusion coefficient ratio instead of mass ratio.

Let us conclude this section with a schematic overview of the assumed mechanism for surface growth of the deposit – it is illustrated in **Figure S4**-*left*. In **Figure S4**-*right*, an idea is given of how this mechanism will alter in the case where most of the oxidation process follows intramolecular propagation reaction.

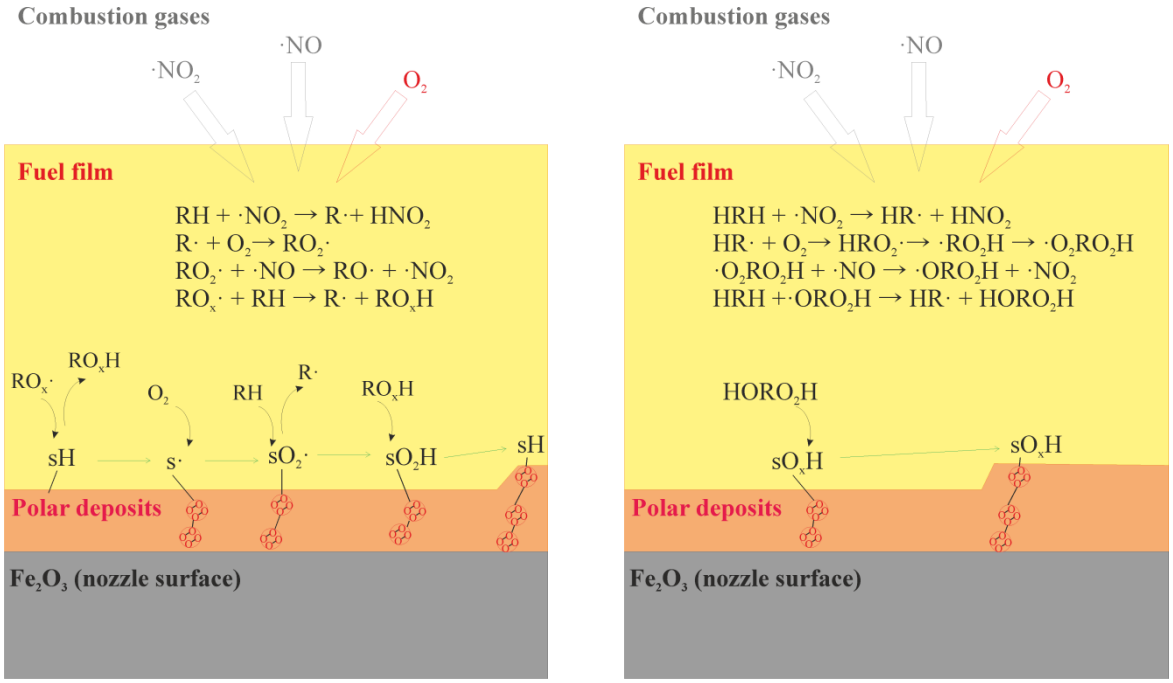

Figure S4-*left*: Mechanism of deposit formation through liquid phase oxidation. Combustion gases provide oxygen and radicals i· that are transferred to the liquid fuel film, reaction (39), and initiate there the radical chain reactions (4). The major radicals in the fuel film (RO_2·, RO· & ·NO_2), start the process of surface oxidation through Eq (18), which leads to deposit oxidation and formation of a polar site sO_xH at the surface, Eq (19). Polar oxidation products adsorb at the active sites and lead to deposit growth. *Right*: in the case where polyfunctional oxidation products are formed in the fuel (HO_2RO_2H) through intramolecular propagation, the site formation and the adsorption stages merge in one, skipping the slow surface initiation stage.

S3. Gas transfer to the liquid film

The transfer process is schematically given by:

$$\mathrm{i}\cdot^{\mathrm{G}} \rightarrow \mathrm{i}\cdot^{\mathrm{S}} \rightarrow \mathrm{i}\cdot\,, \tag{39}$$

where i· refers to the liquid film, $\mathrm{i}\cdot^{\mathrm{S}}$ – to the gas right next to the fuel|gas interface and $\mathrm{i}\cdot^{\mathrm{G}}$ – to the gas deep in the quench layer. If the liquid film is homogeneous in composition (due to efficient turbulent convection, Marangoni effect etc.), the rate of the process is controlled by the following mass balance equation:

$$\frac{\mathrm{d}(V^{\mathrm{F}}[\mathrm{i}\cdot])}{\mathrm{d}t} = A^{\mathrm{F}} j_{\mathrm{i,cond}} - A^{\mathrm{F}} j_{\mathrm{i,evap}} - V^{\mathrm{F}} \nu_{\mathrm{i}}\,; \tag{40}$$

here, A^{F} and V^{F} are the area and the volume of the liquid film; $j_{\mathrm{i,cond}}$ is the current of radicals from the gas phase reaching the liquid|gas interface. If the turbulent convective flux of radicals in the combustion gases is fast enough, $j_{\mathrm{i,cond}}$ is given by the Maxwell-Hertz-Knudsen flux

$$j_{\mathrm{i,cond}} = [\mathrm{i}\cdot]^{\mathrm{S}} \sqrt{\frac{RT}{2\pi M_{\mathrm{i}}}}\,. \tag{41}$$

Here, M_{i} is the molar mass of i·; the factor for the effective hits is assumed equal to one (for heavy molecules it may be smaller). The current $j_{\mathrm{i,evap}}$ in Eq (40) stands for the radicals that evaporate back to the gas phase. Since if Henry's equilibrium is reached it is valid that $j_{\mathrm{i,evap}} = j_{\mathrm{i,cond}}$, we can express $j_{\mathrm{i,evap}}$ through $j_{\mathrm{i,cond}}$ and Henry's constant $K_{\mathrm{H,i}} = [\mathrm{i}\cdot]_{\mathrm{eq}}/[\mathrm{i}\cdot]^{\mathrm{S}}_{\mathrm{eq}}$ of the radical as follows:

$$j_{\mathrm{i,evap}} = \frac{1}{K_{\mathrm{H,i}}} \sqrt{\frac{RT}{2\pi M_{\mathrm{i}}}} [\mathrm{i}\cdot]\,. \tag{42}$$

In the case where the quench layer is polarized, $[\mathrm{i}\cdot]^{\mathrm{S}}$ will be lower than the bulk value $[\mathrm{i}\cdot]^{\mathrm{G}}$; this effect is in part accounted for by our zone transport model (the quench layer is of different composition from that in the cylinder), but additional polarization can be expected due to the convection caused by the mobile liquid interface of the tip-attached droplet, unrelated to the gas mixing rate and the ξ parameter. Assuming that the transport process is described by diffusion trough a stagnant gas layer of thickness L_{st} (beyond which the convection homogenizes the quench layer completely), one can write for the transport rate

$$j_{\mathrm{i}} = D_{\mathrm{i}} \frac{[\mathrm{i}\cdot]^{\mathrm{G}} - [\mathrm{i}\cdot]^{\mathrm{S}}}{L_{\mathrm{st}}}\,. \tag{43}$$

The mass balance of i· at the interface requires that $j_{\mathrm{i}} = j_{\mathrm{i,cond}} - j_{\mathrm{i,evap}}$ which can be written in the form:

$$[\mathrm{i}\cdot]^{\mathrm{S}} - [\mathrm{i}\cdot]/K_{\mathrm{H,i}} = \left(1 + \frac{L_{\mathrm{st}}}{D}\sqrt{\frac{RT}{2\pi M_{\mathrm{i}}}}\right)^{-1} \left([\mathrm{i}\cdot]^{\mathrm{G}} - [\mathrm{i}\cdot]/K_{\mathrm{H,i}}\right). \tag{44}$$

Assuming for simplicity that the fuel film thickness and area are not time dependent, we can then write Eq (40) as

$$\frac{\mathrm{d}[\mathrm{i}\cdot]}{\mathrm{d}t} = \sqrt{\frac{RT}{2\pi M_{\mathrm{i}}}} \frac{[\mathrm{i}\cdot]^{\mathrm{S}} - [\mathrm{i}\cdot]/K_{\mathrm{H,i}}}{h^{\mathrm{F}}} - \nu_{\mathrm{i}} = \frac{1}{\sqrt{\frac{2\pi M_{\mathrm{i}}}{RT}} + \frac{L_{\mathrm{st}}}{D}} \frac{[\mathrm{i}\cdot]^{\mathrm{G}} - [\mathrm{i}\cdot]/K_{\mathrm{H,i}}}{h^{\mathrm{F}}} - \nu_{\mathrm{i}}\,, \tag{45}$$

where we have used that $h^{\mathrm{F}} = V^{\mathrm{F}}/A^{\mathrm{F}}$. It is evident from this equation that if h^{F} is small enough, the concentration [i·] in the liquid phase will be close to the equilibrium value $[\mathrm{i}\cdot] = K_{\mathrm{H,i}}[\mathrm{i}\cdot]^{\mathrm{S}}$. On the other hand, a larger quantity of fuel will result in lower concentration of radicals and eventually, *slower* oxidation process. Various processes can complicate the above equation – thermophoresis (thermodiffusion) is likely, and the unsteady nature of the convection may lead to variation of L_{st} with time.

The initiation rate is given by Eq (5), which, if one initiator dominates the process, simplifies to $v_\mathrm{i} = k_\mathrm{i}[\mathrm{RH}][\mathrm{i}\cdot]$. If during the degradation the temperature of the film is fixed to the constant T_tip, the solution to Eq (45) reads:

$$[\mathrm{i}\cdot] = \frac{K_{\mathrm{H,i}}}{\tau_\mathrm{tr}} \int_0^t [\mathrm{i}\cdot]^\mathrm{G} \exp\left[-\left(t-t'\right)\left(\frac{1}{\tau_\mathrm{i}} + \frac{1}{\tau_\mathrm{tr}} \right) \right] \mathrm{d}t' , \tag{46}$$

where we introduced the characteristic times τ_tr of the transport processes and τ_i of the initiation reaction as:

$$\tau_\mathrm{tr} = \tau_\mathrm{M} + \tau_\mathrm{st} = K_{\mathrm{H,i}} h^\mathrm{F} \sqrt{\frac{2\pi M_\mathrm{i}}{RT}} + \frac{K_{\mathrm{H,i}} h^\mathrm{F} L_\mathrm{st}}{D} \quad \text{and} \quad \tau_\mathrm{i} = \frac{1}{k_\mathrm{i}[\mathrm{RH}]}, \tag{47}$$

where $K_{\mathrm{H,i}} h^\mathrm{F} (2\pi M_\mathrm{i}/RT)^{1/2}$ stands for the contribution of the Hertz-Knudsen-Maxwell transfer through the interface and $K_{\mathrm{H,i}} h^\mathrm{F} L_\mathrm{st}/D$ relates to the convective diffusion rate. Their orders of magnitude for NO_2 are τ_M ~ 0.5-1 μs, τ_st = 20-50 μs (for L_st ~ 1 μm) and τ_i = 5-50 ms in the range T_tip = 140-190°C. As τ_tr is small compared to the time of the cycle (~1 ms), only a tiny range of times close to $t' \sim t$ contributes to the integral (46), which allows us to simplify it:

$$[\mathrm{i}\cdot] \approx \frac{K_{\mathrm{H,i}}}{\tau_\mathrm{tr}} \int_0^t [\mathrm{i}\cdot]^\mathrm{G}_{t'=t} \exp\left[-\left(t-t'\right)\left(\frac{1}{\tau_\mathrm{i}} + \frac{1}{\tau_\mathrm{tr}} \right) \right] \mathrm{d}t' \approx \frac{\tau_\mathrm{i}}{\tau_\mathrm{i} + \tau_\mathrm{tr}} K_{\mathrm{H,i}} [\mathrm{i}\cdot]^\mathrm{G} . \tag{48}$$

In addition, $\tau_\mathrm{i} >> \tau_\mathrm{tr}$, therefore

$$[\mathrm{i}\cdot] = K_{\mathrm{H,i}} [\mathrm{i}\cdot]^\mathrm{G} . \tag{49}$$

We present this derivation in order to analyse the limits of validity of Eq (49). There are two cases in which Eq (49) would fail. For heavy radicals with high affinity to the fuel phase (large $K_{\mathrm{H,i}}$), τ_tr can have value comparable will the period of the cycle. Then, the flux through the interface will not have enough time to equilibrate the liquid, leading to lower concentration of these radicals in the fuel. Also, very reactive radicals (such as RO·) may have τ_i much smaller than τ_tr. In this case, instead of Eq (49), one must use Eq (48), which predicts lower concentration of these radicals in the bulk compared to the equilibrium one. Both effects diminish the role of large, reactive radicals produced by the combustion.

Let us estimate the magnitude of a related effect: when the fuel film is close to its boiling point, its vapour pressure is close to that of the ambient gas and the vapours released by it in the quench layer dilute the gas components near the interface. Let the fuel F saturate the gas phase right next to the surface ($p_\mathrm{eq} = RT[\mathrm{F}]^\mathrm{S}$ is the vapour pressure of F), while its concentration at the exit of the stagnated layer is negligibly low, $[\mathrm{F}]^\mathrm{G} \approx 0$. The total concentration of other gases in the stagnant layer (mostly N_2, O_2, CO_2) is fixed by the ideal gas and Dalton's laws, $[\mathrm{G}] = p/RT - [\mathrm{F}]$. The fluxes of [G] and [F] through the stagnant layer, neglecting for simplicity the difference in their diffusion coefficients, are given by:

$$j_\mathrm{F} = -D\frac{\mathrm{d}[\mathrm{F}]}{\mathrm{d}z} + [F]v , \quad j_\mathrm{G} = +D\frac{\mathrm{d}[\mathrm{F}]}{\mathrm{d}z} + \left(\frac{p}{RT} - [F] \right) v << j_\mathrm{F} ; \tag{50}$$

the amount of gases G passing through the interface is, strictly speaking, not zero (as some gas dissolves into the fuel), but this amount is small compared to the evaporative flux j_F. Therefore, the gas velocity v can be calculated from the second equation as:

$$v \approx -\frac{D}{\frac{p}{RT} - [F]} \frac{\mathrm{d}[\mathrm{F}]}{\mathrm{d}z} . \tag{51}$$

Thus, the fuel vapours drive a gas flow in the quench layer in direction towards the cylinder. Using Eqs (50)&(51), and the mass balance $\mathrm{d}j_\mathrm{F}/\mathrm{d}z = 0$, one can obtain a solution for [F](z) and the respective flux of fuel:

$$[\mathrm{F}] = \frac{p}{RT}\left[1-\left(1-\frac{p_{\mathrm{eq}}}{p}\right)^{1-z/L_{\mathrm{st}}}\right], \quad j_{\mathrm{F}} = -\frac{Dp}{L_{\mathrm{st}}RT}\ln\left(1-\frac{p_{\mathrm{eq}}}{p}\right). \tag{52}$$

If the leakage rate were known, the second result could be used to predict the amount of leaked fuel as function of time. From the first equation and Dalton's law, it follows that the ambient gas concentration right next to the wall falls to a value of $[\mathrm{G}]^{\mathrm{S}} = (p - p_{\mathrm{eq}})/RT$ and approaches zero near the boiling point (where $p_{\mathrm{eq}} = p/RT$). By substituting Eq (52) into Eq (51), we obtain an expression for the gas velocity caused by the diluting fuel vapour flux:

$$v = -\frac{D}{L_{\mathrm{st}}}\ln\left(1-\frac{p_{\mathrm{eq}}}{p}\right). \tag{53}$$

This velocity is constant (which will not be the case if the difference in diffusion coefficients is taken into account).

For the initiator, under the assumption that it is a minor component, one can write

$$j_{\mathrm{i}} = -D_{\mathrm{i}}\frac{\mathrm{d}[\mathrm{i}\cdot]}{\mathrm{d}z} + [\mathrm{i}\cdot]v. \tag{54}$$

The mass balance $\mathrm{d}j_{\mathrm{i}}/\mathrm{d}z = 0$, together with the boundary conditions $[\mathrm{i}\cdot](z = 0) = [\mathrm{i}\cdot]^{\mathrm{S}}$ and $[\mathrm{i}\cdot](z = L_{\mathrm{st}}) = [\mathrm{i}\cdot]^{\mathrm{G}}$, leads to the final result

$$j_{\mathrm{i}} = -\left[\left([\mathrm{i}\cdot]^{\mathrm{G}} - [\mathrm{i}\cdot]^{\mathrm{S}}\right)\frac{p}{p_{\mathrm{eq}}} - [\mathrm{i}\cdot]^{\mathrm{G}}\right]\frac{D}{L_{\mathrm{st}}}\ln\left(1-\frac{p_{\mathrm{eq}}}{p}\right). \tag{55}$$

Although approximate, this result can be used to analyse the limitations of the assumption for negligible dilution of the quench layer by the fuel vapours. If $p_{\mathrm{eq}} << p$, the above flux simplifies to Eq (43) and the analysis above is correct. Even when the two pressures do not differ much (e.g., $p_{\mathrm{eq}} \sim 0.8p$), the correction for this effect is unimportant as long as $\tau_{\mathrm{tr}} << \tau_{\mathrm{i}}$ and τ_{tr} is small compared to the cycle period, since j_{i} would correspond to a relatively fast transport anyway. However, when p_{eq} approaches p nearby CAD_0 and $\mathrm{CAD}_{\mathrm{b}}$, the flux j_{i} will become so slow that the transport time will approach τ_{i} or the cycle time. The result is that some 10 CAD after CAD_0 and 10 CAD before $\mathrm{CAD}_{\mathrm{B}}$, the rate of delivery of radicals to the film can be expected to be significantly reduced. At low temperatures (below ~180°C), this will have little effect on the deposition rate because these time intervals do not contribute to the deposition (cf. **Figure 3**). However, at higher tip temperatures, p_{eq} will be large (so the magnitude of the dilution effect will be significant), and in addition, the boiling range is shorter, cf. Figure S1, meaning that the proportion of the CAD range affected by the dilution will be significant. Therefore, the results in Sec. 2.3 for the deposition rates are overestimating the true rates at $T \geq 180$°C.

S4. Nozzle channel deposits: relationship between flow reduction and deposit thickness, and processing of the experimental data

Let us first analyse the accuracy of the relation $1 - Q/Q_0 \approx 2h_{\mathrm{n}}/R_{\mathrm{n}}$, Eq (27). Toward this goal, we first consider the Colebrook-White equation (which has been proposed for long channels, but involves roughness explicitly). Its original formulation is via a non-linear equation for the Darcy friction factor f:

$$\frac{1}{\sqrt{f}} = -2\lg\left[\frac{\varepsilon}{7.4\left(R_{\mathrm{n}} - h_{\mathrm{n}}\right)} + \frac{2.51}{Re\sqrt{f}}\right]. \tag{56}$$

The relation between the discharge per unit area $Q/\pi(R_n-h_n)^2$ (the average velocity of the fuel) and the driving force of the flow (the pressure gradient $\Delta p/L$, where L is the nozzle channel length) involves f:

$$\frac{\Delta p}{L}=\frac{f\rho^F}{4(R_n-h_n)}\left[\frac{Q}{\pi(R_n-h_n)^2}\right]^2 . \quad (57)$$

In the above, the Reynolds number stands for:

$$Re=\frac{2\rho^F(R_n-h_n)}{\eta^F}\frac{Q}{\pi(R_n-h_n)^2} . \quad (58)$$

Eqs (56)-(58) set system of equations that allows the calculation of Q, f & Re if the roughness ε and the thickness h are known. The expansion into series of $1-Q/Q_0$, Q being the solution of Eqs (56)-(58) and Q_0 being Q at $h_n = 0$, with respect to small h_n yields:

$$1-\frac{Q}{Q_0}=\frac{5}{2}\frac{h_n}{R_n}-\frac{\dfrac{\varepsilon}{7.4R_n}+\dfrac{3}{2}\dfrac{0.628\eta^F}{R_n^{3/2}\sqrt{\rho^F\Delta p/L}}}{\left(\dfrac{\varepsilon}{7.4R_n}+\dfrac{0.628\eta^F}{R_n^{3/2}\sqrt{\rho^F\Delta p/L}}\right)\ln\left(\dfrac{\varepsilon}{7.4R_n}+\dfrac{0.628\eta^F}{R_n^{3/2}\sqrt{\rho^F\Delta p/L}}\right)}\frac{h_n}{R_n} . \quad (59)$$

For the typical parameters of fuel injection, the first term dominates; neglecting the second, we arrive at the relation $1-Q/Q_0 \approx 5h_n/2R_n$ (corresponding to $\partial\ln C_d/\partial R_n \approx 0.5/R_n$ in Eq (27)). As for the $\partial\ln C_d/\partial\varepsilon$ term in Eq (27), for a 50 μm nozzle, from Eqs (56)-(58) it can be shown that it is approximately $\partial\ln C_d/\partial\varepsilon \approx -0.07/\varepsilon$. As the deposits grow in the grooves of the metal surface, they decrease the roughness and it can be assumed that $d\varepsilon/dh_n \approx -1$. As $\varepsilon << R_n$, the roughness term in Eq (27) will dominate and so the deposits should cause a significant increase of the flow rate during this initial period. Once the surface is covered by deposits, ε of the deposit|fuel interface should not change with h_n and so $d\varepsilon/dh_n = 0$. Therefore, the result $1-Q/Q_0 \approx 2h_n/R_n$ can be used only after the metal grooves are already filled with deposits.

Another empirical formula that is often used for discharge through orifices [62] is:

$$C_d=\left[1.5+9.72\frac{L_n^{1/2}}{(R_n-h_n)^{1/2}Re^{1/2}}\right]^{-1/2} . \quad (60)$$

For the typical range of values of Re, L_n and R_n of a fuel injector, it yields $\partial\ln C_d/\partial R_n \approx 0.05$-$0.1/R_n$, lower than $0.5/R_n$ following from Eq (59). Therefore, the error of the relation $1-Q/Q_0 \approx 2h_n/R_n$ that follows from Eqs (59)&(60) is less than 20%, which is acceptable for the purposes of this work.

We use the relation (27) to transform the experimental data of Aradi et al. [50] for the rate of deposit growth from relative to absolute values. After careful investigation of *figures 17&13* of Aradi et al., we concluded that for the regression, they used the formula $v_n/k_r\times(1-e^{-v_n t})$ instead of their correct *eq 11* (our Eq (25)). In result, in the v_n-column (their k_1) of *table 5* [50], what actually stands are the values of k_r (their k_2). In the second, k_r-column (their k_2) of *table 5*, the data refer actually to the quantity $R_n k_r^2/2v_n$ (where the factor $2/R_n$ occurs as h_n is made dimensionless via division by $R_n/2$, as it follows from *eq 10* in [50]). Thus, to compare their experimental results with our theoretical v_n, we must use $k_1^2/k_2\times R_n/2$, with k_1 and k_2 from *table 5* [50]. Unfortunately, they did not provide value for R_n, so we assumed $R_n = 50$ μm. To compare our results with the experimental data, we recalculated the correct coefficients in **Table S3** for the data for non-additized fuels. In addition, one of the fuels used by Aradi formed deposits after a relatively clear induction period, **Figure S5**-right, probably due to the anti-oxidant effect

of the sulfur compounds present in that fuel [79]. In this case, instead of Eq (25), we used for h_n a modified expression to fit the data of Aradi et al.:

$$h_n = \frac{v_n}{k_r}\left[1 - e^{-k_r(t-t_{ind})}\right], \qquad (61)$$

where t_{ind} is the induction time of the deposition process, which is non-zero in the presence of anti-oxidants. The fit of Aradi et al. is compared with the one with Eq (61) in **Figure S5**-right. The respective parameters of the deposition are compared in **Table S3**: both k_r and v_n have more reasonable values if induction time is allowed for.

Table S3: The data of Aradi et al. [50] for the flow rate reduction due to nozzle channel deposits – calculation of the correct rate parameters v_n & k_r.

[a] Fuel	$T_{90\%}$ [°C]	Olefin [*w*%]	Arenes [*v*%]	S [*w*ppm]	[b] k_1 [h^{-1}]	[b] k_2 [h^{-1}]	[c] k_r [h^{-1}]	[d] v_n from Eq (27) [μm/h]
Howell-EEE	160	1.2	30.6	20	0.53	4.57	0.535	1.5648
Fuel 7	161	19.9		153	0.57	8.76	0.568	0.9208
Fuel 10	171	12.9		421	0.103	0.427	0.103	0.6211
							[e]0.55	[e]1.53
[f] PR4915 (ULG95/E5)	157	3	35	<10	-	-	[g]0.30	[g]0.23

[a] For details cf. Refs. [50,78].
[b] Values from *table 5* in Ref. [50].
[c] The correct k_r, equal to k_1.
[d] Deposit formation rate v_n (made in units μm/h) calculated as $k_1^2/k_2 \times R_n/2$. The unit conversion involves the relation (27), $1-Q/Q_0 \approx 2h_n/R_n$.
[e] These values have been obtained by assuming induction time of the deposition process, t_{ind} = 1.2 h, due to the anti-oxidant effect of the sulfur compounds. Eq (61) was used to fit the data of Aradi et al. instead of Eq (25).
[f] This fuel contains also 10% oxygenates.
[g] Obtained by fitting the data from Ref. [78] with Eq (30), cf. in **Figure S6**.

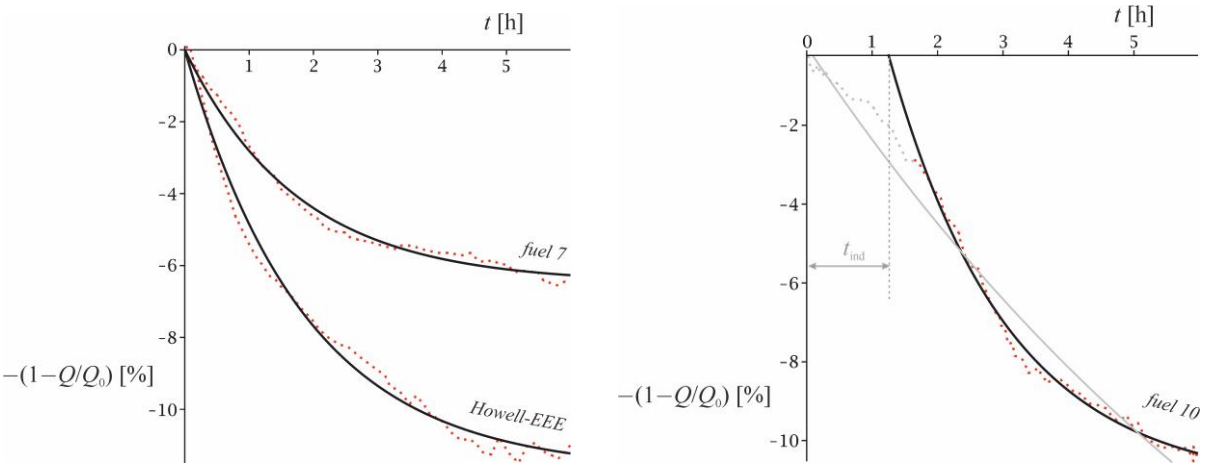

Figure S5 *left*: comparison between data of Aradi et al. for the reduction of the flow rate for two fuels (red dot lines) with the model (25) with the parameters from Table S3 (black lines). *Right*: the dot line is data by Aradi et al.; the gray line is the model (25) with the parameter values of Aradi et al.; the black line is the model (61) with induction time of 1.2 h due to the anti-oxidant effect of the sulfur compounds present (cf. Table S3 for details).

We used Eq (30) also to fit the data for the signal time presented by Jiang et al. [78]. The results are given in **Figure S6** and **Table S3** (we used R_n = 80 μm as obtained from the image in *fig. 6* of Ref. [78]). The test of Jiang et al. was complicated, however, by soaking periods and cold starts. From the data, it seems that 1-2 hours of the test after each cold start are affected

reversibly by the soaking and the cold start; after that, the test continues as if only the slow deposition process plays a role. Therefore, we neglected these initial periods for the regression (as depicted in Figure S6). The 4th cold start of Jiang et al., however, had a lasting effect which can be interpreted as a chunk of the deposit being removed from the nozzle channel (this is a common phenomenon [50]). We therefore neglected also the 4th, 5th and 6th cold starts. An additional problem is that the temperature of the injector has not been reported by Jiang et al.

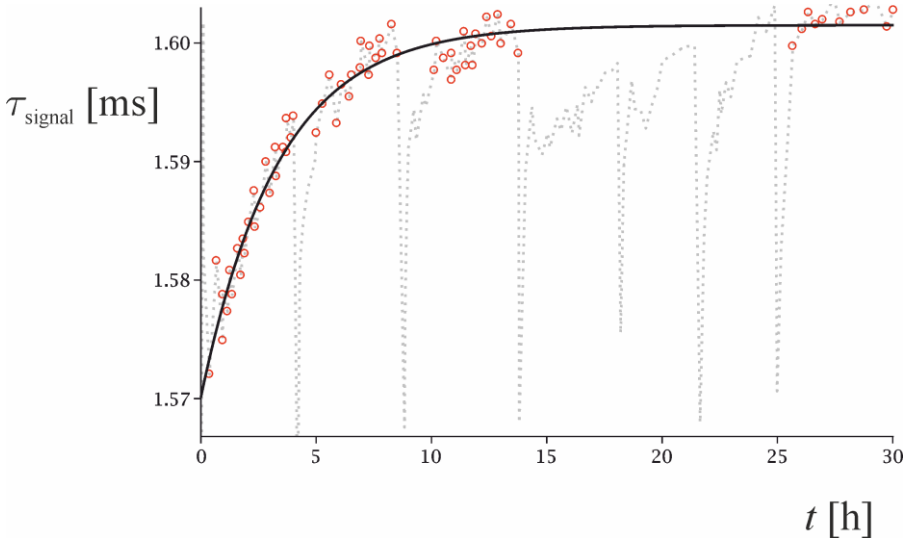

Figure S6: data for the injection signal time at fixed injection mass as function of engine operation time by Jiang et al. [78] (gray dot line and red points). Black line is the model (30) with the parameters in Table S3. The test involved soaking periods, which affected 1-2 hours after each engine cold start; the respective data have been ignored. The 4th cold start had a lasting effect and the data for the 3 subsequent starts have also been ignored, cf. the text.

S5. The multilayer heat transfer problem

We solve the heat transfer problem set by Fourier's equations for the metal and the deposit phase:

$$-h^{\mathrm{M}} < z < 0: \quad \frac{\partial T^{\mathrm{M}}}{\partial t} = \chi^{\mathrm{M}} \frac{\partial^2 T^{\mathrm{M}}}{\partial z^2} \; ;$$
$$0 < z < h_{\mathrm{tip}}: \quad \frac{\partial T^{\mathrm{D}}}{\partial t} = \chi^{\mathrm{D}} \frac{\partial^2 T^{\mathrm{D}}}{\partial z^2} \; . \qquad (62)$$

The heat current q^{S} coming from the gas phase is a periodic function obtained by the engine simulation and illustrated in Figure S7. The Fourier series of it is:

$$\left(\kappa^{\mathrm{D}} \frac{\partial T^{\mathrm{D}}}{\partial z}\bigg|_{z=h_{\mathrm{tip}}} = \right) \quad q^{\mathrm{S}} = \bar{q}^{\mathrm{S}} + \sum_{n=1}^{N} q^{\mathrm{S}}_{\mathrm{c},n} \cos n\omega t + \sum_{n=1}^{N} q^{\mathrm{S}}_{\mathrm{s},n} \sin n\omega t \, , \qquad (63)$$

where

$$\bar{q}^{\mathrm{S}} = \frac{1}{\tau} \int_{-\tau/2}^{\tau/2} q^{\mathrm{S}} \mathrm{d}t \, , \quad q^{\mathrm{S}}_{\mathrm{c},n} = \frac{2}{\tau} \int_{-\tau/2}^{\tau/2} q^{\mathrm{S}} \cos n\omega t \mathrm{d}t \, , \text{ and } \quad q^{\mathrm{S}}_{\mathrm{s},n} = \frac{2}{\tau} \int_{-\tau/2}^{\tau/2} q^{\mathrm{S}} \sin n\omega t \mathrm{d}t \qquad (64)$$

are the Fourier coefficients of $q^{\mathrm{S}}(t)$. The angular frequency ω is related to the period as $\omega = 2\pi/\tau$. As it follows from Eq (64), the coefficient $\bar{q}^{\mathrm{S}}$ is precisely the average heat flux to the wall

(0.156 MW/m^2 for the data in Figure S7). Eq (63) is the first boundary condition for Eq (62). The other three are:

$$z = 0: \qquad T^{\mathrm{M}} = T^{\mathrm{D}} \quad \text{and} \quad \kappa^{\mathrm{M}} \frac{\partial T^{\mathrm{M}}}{\partial z} = \kappa^{\mathrm{D}} \frac{\partial T^{\mathrm{D}}}{\partial z} \; ;$$
$$z = -h^{\mathrm{M}}: \qquad T^{\mathrm{M}} = T_{\mathrm{out}}. \tag{65}$$

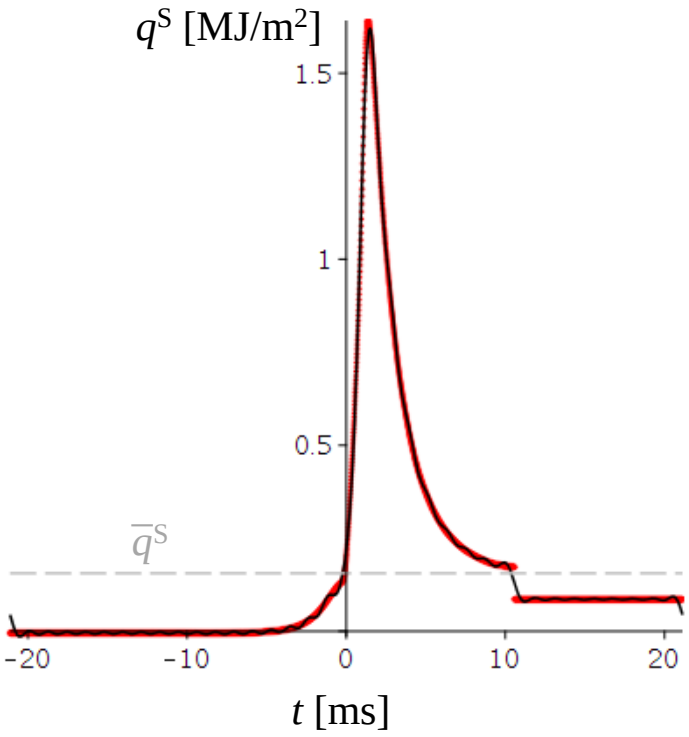

Figure S7: Heat flux from the cylinder charge to the injector wall during a cycle as a function of time. Red: simulation data; black– the Fourier series (63), N = 36. Grey – the average flux $\overline{q}^{\mathrm{S}}$, Eq (64).

The solution to the stated problem reads:

$$T^{\mathrm{M}} = \bar{T}^{\mathrm{M}}(z) + \sum_{n=1}^{N} T^{\mathrm{M}}_{\mathrm{c},n}(z) \cos n\omega t + \sum_{n=1}^{N} T^{\mathrm{M}}_{\mathrm{s},n}(z) \sin n\omega t \, ,$$
$$T^{\mathrm{D}} = \bar{T}^{\mathrm{D}}(z) + \sum_{n=1}^{N} T^{\mathrm{D}}_{\mathrm{c},n}(z) \cos n\omega t + \sum_{n=1}^{N} T^{\mathrm{D}}_{\mathrm{s},n}(z) \sin n\omega t \, . \tag{66}$$

Here, the Fourier coefficients of $T(z,t)$ are related to those of q^{S}. The 0$^{\mathrm{th}}$-order coefficients are related via Eqs (31)-(32). The functional dependence of the four Fourier coefficients $T^{\mathrm{M}}_{\mathrm{c},n}$, $T^{\mathrm{M}}_{\mathrm{s},n}$, $T^{\mathrm{D}}_{\mathrm{c},n}$ and $T^{\mathrm{D}}_{\mathrm{s},n}$ on z follows from the Fourier series of Eqs (62). For the deposit phase,

$$T^{\mathrm{M}}_{\mathrm{c},n} \approx \left(c^{\mathrm{M}}_{1,n} \cos \frac{z}{\delta^{\mathrm{M}}_n} + c^{\mathrm{M}}_{3,n} \sin \frac{z}{\delta^{\mathrm{M}}_n} \right) \mathrm{e}^{-|z|/\delta^{\mathrm{M}}_n} \; ;$$
$$T^{\mathrm{M}}_{\mathrm{s},n} \approx \left(-c^{\mathrm{M}}_{1,n} \sin \frac{z}{\delta^{\mathrm{M}}_n} + c^{\mathrm{M}}_{3,n} \cos \frac{z}{\delta^{\mathrm{M}}_n} \right) \mathrm{e}^{-|z|/\delta^{\mathrm{M}}_n} \; ;$$
$$T^{\mathrm{D}}_{\mathrm{c},n} = \left(c^{\mathrm{D}}_{1,n} \cos \frac{z}{\delta^{\mathrm{D}}_n} + c^{\mathrm{D}}_{3,n} \sin \frac{z}{\delta^{\mathrm{D}}_n} \right) \mathrm{e}^{-z/\delta^{\mathrm{D}}_n} + \left(c^{\mathrm{D}}_{2,n} \cos \frac{z}{\delta^{\mathrm{D}}_n} + c^{\mathrm{D}}_{4,n} \sin \frac{z}{\delta^{\mathrm{D}}_n} \right) \mathrm{e}^{z/\delta^{\mathrm{D}}_n} \; ;$$

$$T^{\mathrm{D}}_{\mathrm{s},n} = \left(c^{\mathrm{D}}_{1,n} \sin\frac{z}{\delta^{\mathrm{D}}_n} - c^{\mathrm{D}}_{3,n} \cos\frac{z}{\delta^{\mathrm{D}}_n} \right) \mathrm{e}^{-z/\delta^{\mathrm{D}}_n} + \left(-c^{\mathrm{D}}_{2,n} \sin\frac{z}{\delta^{\mathrm{D}}_n} + c^{\mathrm{D}}_{4,n} \cos\frac{z}{\delta^{\mathrm{D}}_n} \right) \mathrm{e}^{z/\delta^{\mathrm{D}}_n} . \qquad (67)$$

Here, the characteristic lengths of the heat transfer in the metal and in the deposit phase are:

$$\delta^{\mathrm{M}}_n = \sqrt{2\chi^{\mathrm{M}}/n\omega} \quad \text{and} \quad \delta^{\mathrm{D}}_n = \sqrt{2\chi^{\mathrm{D}}/n\omega} . \qquad (68)$$

The Fourier coefficients of T in the metal phase contain, in principle, a second term proportional to $\exp(+|z|/\delta^{\mathrm{M}}_n)$, but the coefficients multiplying it can be shown to be negligible (proportional to the small $\exp(-h^{\mathrm{M}}/\delta^{\mathrm{M}}_n)$) and are consequently neglected in Eq (67). Therefore, the oscillating part of T^{M} decays fast with z, which means that near the outer wall of the metal, the temperature follows almost exactly the stationary linear profile $\bar{T}^{\mathrm{M}}(z)$, cf. Eq (31).

The c-coefficients in Eq (67) follow from the Fourier series of the boundary conditions (63)-(65) (without the last). For each i, from the temperature continuity at $z = 0$ it follows that:

$$\begin{aligned} -c^{\mathrm{D}}_{3,n} + c^{\mathrm{D}}_{4,n} &= c^{\mathrm{M}}_{3,n} ; \\ c^{\mathrm{D}}_{1,n} + c^{\mathrm{D}}_{2,n} &= c^{\mathrm{M}}_{1,n} . \end{aligned} \qquad (69)$$

From the heat flux continuity,

$$\begin{aligned} \frac{\kappa^{\mathrm{D}}}{\delta^{\mathrm{D}}_n} \left(c^{\mathrm{D}}_{1,n} - c^{\mathrm{D}}_{2,n} + c^{\mathrm{D}}_{3,n} + c^{\mathrm{D}}_{4,n} \right) &= \frac{\kappa^{\mathrm{M}}}{\delta^{\mathrm{M}}_n} \left(-c^{\mathrm{M}}_{1,n} + c^{\mathrm{M}}_{3,n} \right) ; \\ \frac{\kappa^{\mathrm{D}}}{\delta^{\mathrm{D}}_n} \left(-c^{\mathrm{D}}_{1,n} + c^{\mathrm{D}}_{2,n} + c^{\mathrm{D}}_{3,n} + c^{\mathrm{D}}_{4,n} \right) &= \frac{\kappa^{\mathrm{M}}}{\delta^{\mathrm{M}}_n} \left(c^{\mathrm{M}}_{1,n} + c^{\mathrm{M}}_{3,n} \right) . \end{aligned} \qquad (70)$$

The solution to Eqs (69)-(70) reads:

$$\begin{aligned} c^{\mathrm{M}}_{1,n} &= \frac{2\kappa^{\mathrm{D}}/\delta^{\mathrm{D}}_n}{\kappa^{\mathrm{D}}/\delta^{\mathrm{D}}_n - \kappa^{\mathrm{M}}/\delta^{\mathrm{M}}_n} c^{\mathrm{D}}_{1,n} ; \quad c^{\mathrm{M}}_{3,n} = -\frac{2\kappa^{\mathrm{D}}/\delta^{\mathrm{D}}_n}{\kappa^{\mathrm{D}}/\delta^{\mathrm{D}}_n - \kappa^{\mathrm{M}}/\delta^{\mathrm{M}}_n} c^{\mathrm{D}}_{3,n} ; \\ c^{\mathrm{D}}_{2,n} &= \frac{\kappa^{\mathrm{D}}/\delta^{\mathrm{D}}_n + \kappa^{\mathrm{M}}/\delta^{\mathrm{M}}_n}{\kappa^{\mathrm{D}}/\delta^{\mathrm{D}}_n - \kappa^{\mathrm{M}}/\delta^{\mathrm{M}}_n} c^{\mathrm{D}}_{1,n} ; \quad c^{\mathrm{D}}_{4,n} = -\frac{\kappa^{\mathrm{D}}/\delta^{\mathrm{D}}_n + \kappa^{\mathrm{M}}/\delta^{\mathrm{M}}_n}{\kappa^{\mathrm{D}}/\delta^{\mathrm{D}}_n - \kappa^{\mathrm{M}}/\delta^{\mathrm{M}}_n} c^{\mathrm{D}}_{3,n} . \end{aligned} \qquad (71)$$

From the flux continuity (63) at $z = h^{\mathrm{D}}$, the last two coefficients of the n^{th} order follow:

$$\begin{aligned} c^{\mathrm{D}}_{3,n} &= \left(1 - \frac{\kappa^{\mathrm{M}}\delta^{\mathrm{D}}_n}{\kappa^{\mathrm{D}}\delta^{\mathrm{M}}_n} \right) \frac{\left(A_{+-} + A_{-+} \right) q^{\mathrm{S}}_{\mathrm{s},n} - \left(A_{++} + A_{--} \right) q^{\mathrm{S}}_{\mathrm{c},n}}{\left(A_{+-} + A_{-+} \right)^2 + \left(A_{++} + A_{--} \right)^2} ; \\ c^{\mathrm{D}}_{1,n} &= -\left(1 - \frac{\kappa^{\mathrm{M}}\delta^{\mathrm{D}}_n}{\kappa^{\mathrm{D}}\delta^{\mathrm{M}}_n} \right) \frac{\left(A_{++} + A_{--} \right) q^{\mathrm{S}}_{\mathrm{s},n} + \left(A_{+-} + A_{-+} \right) q^{\mathrm{S}}_{\mathrm{c},n}}{\left(A_{+-} + A_{-+} \right)^2 + \left(A_{++} + A_{--} \right)^2} , \end{aligned} \qquad (72)$$

where

$$\begin{aligned} A_{++} &= \left(\sin\frac{h_{\mathrm{tip}}}{\delta^{\mathrm{D}}_n} + \cos\frac{h_{\mathrm{tip}}}{\delta^{\mathrm{D}}_n} \right) \left(\frac{\kappa^{\mathrm{D}}}{\delta^{\mathrm{D}}_n} + \frac{\kappa^{\mathrm{M}}}{\delta^{\mathrm{M}}_n} \right) \mathrm{e}^{h_{\mathrm{tip}}/\delta^{\mathrm{D}}_n} ; \\ A_{-+} &= \left(\sin\frac{h_{\mathrm{tip}}}{\delta^{\mathrm{D}}_n} - \cos\frac{h_{\mathrm{tip}}}{\delta^{\mathrm{D}}_n} \right) \left(\frac{\kappa^{\mathrm{D}}}{\delta^{\mathrm{D}}_n} + \frac{\kappa^{\mathrm{M}}}{\delta^{\mathrm{M}}_n} \right) \mathrm{e}^{h_{\mathrm{tip}}/\delta^{\mathrm{D}}_n} ; \\ A_{+-} &= \left(\sin\frac{h_{\mathrm{tip}}}{\delta^{\mathrm{D}}_n} + \cos\frac{h_{\mathrm{tip}}}{\delta^{\mathrm{D}}_n} \right) \left(\frac{\kappa^{\mathrm{D}}}{\delta^{\mathrm{D}}_n} - \frac{\kappa^{\mathrm{M}}}{\delta^{\mathrm{M}}_n} \right) \mathrm{e}^{-h_{\mathrm{tip}}/\delta^{\mathrm{D}}_n} ; \\ A_{--} &= \left(\sin\frac{h_{\mathrm{tip}}}{\delta^{\mathrm{D}}_n} - \cos\frac{h_{\mathrm{tip}}}{\delta^{\mathrm{D}}_n} \right) \left(\frac{\kappa^{\mathrm{D}}}{\delta^{\mathrm{D}}_n} - \frac{\kappa^{\mathrm{M}}}{\delta^{\mathrm{M}}_n} \right) \mathrm{e}^{-h_{\mathrm{tip}}/\delta^{\mathrm{D}}_n} . \end{aligned} \qquad (73)$$

The profile (66) is illustrated in **Figure S8**.

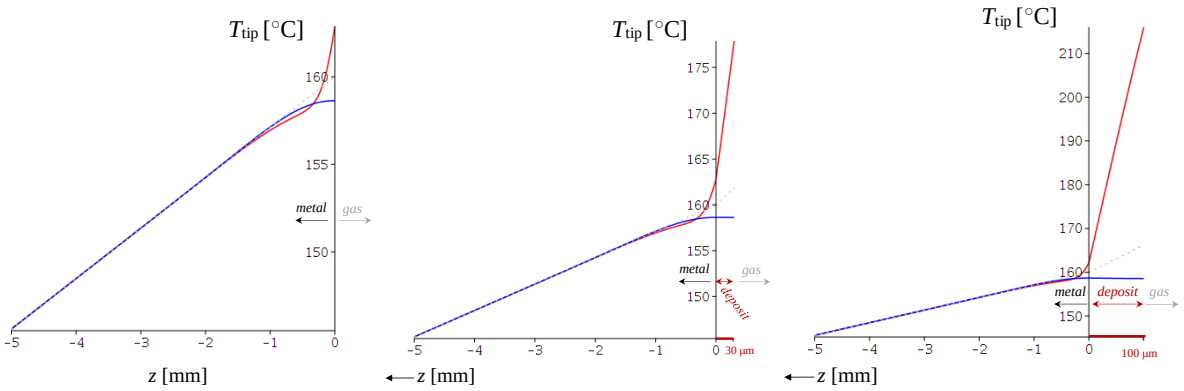

Figure S8: Profiles of the temperature for three values of h_{tip}: 0, 30, 100 µm. The abscissa axis in the positive region of z is multiplied by 10 for clarity.

S6. List of symbols and abbreviations

Symbols

a	fraction of $RO_2\cdot$ that terminate during the reaction between two $RO_2\cdot$, $a = k_t/(k_t + k_{OH})$
a_{sH}	average area per C-H bond at the surface
CAD_0	CAD of start of accumulation of leaked fuel
CAD_b	CAD of boiling and precipitation
C_d	discharge coefficient
c	heat capacity per unit volume of a material
E	activation energy in the Arrhenius law for k
h^F	fuel film thickness
h^M	thickness of the metal layer at the injector surface
h_n	thickness of the nozzle channel deposits
h_{tip}	thickness of the injector tip deposits
Δh	increase of the deposit thickness for the period of one cycle
[i·]	concentration of the initiator in the fuel film
$[i\cdot]^G$	concentration of the initiator in the quench layer
K_H	Henry's constant
k	rate constant
k_0	preexponential factor in the Arrhenius law for k
k_r	empirical proportionality constant in the rate $-k_r h_n$ of deposit removal
L	length of the nozzle channel
M_d	molar mass of the deposit precursors
p	cylinder pressure
p_0	standard pressure, 101325 Pa
p_{eq}	vapour pressure of the fuel
Δp	injector pressure
Q	volumetric flow rate through the nozzle
Q_0	maximal volumetric flow rate through the nozzle
q^S	heat flux from the combustion gases to the injector surface
R	gas constant
R_n	nozzle channel radius (not affected by the deposits)
r_W	Wenzel factor (ratio between actual area of a rough surface and projected area)
sH	deposit-bound reactive C-H bond at the interface deposit|fuel
T	temperature

$T_{90\%}$ T at which 90% of the fuel is evaporated ($T_{90\%} = T_b$ for single component fuel)
T_b boiling temperature
T_{b0} normal boiling temperature at p_0
T^F film temperature, $\min(T_b, T_{tip})$
T_{out} temperature at the outer wall ($x = -h^M$) of the metal layer
T_{tip} injector tip surface temperature
t time
t_0 starting time of the accumulation of leaked fuel, $\tau \times CAD_0/720^\circ$
t_b moment of boiling and precipitation, $\tau \times CAD_b/720^\circ$
t_{end} end of the combustion cycle, $\tau/2$
V volume of the leaked droplet
ν rate of a reaction
ν_i initiation rate [mol/m^{3}s]
ν_n rate of formation of nozzle channel deposits, $\Delta h_n/\tau$
ν^S rate of a reaction at the interface deposit|fuel [mol/m^{2}s]
w% weight part
$w$ppm weigth ppm
x% molar part
$x$ppm molar ppm
x_{active} the fraction of reactive C-H bonds at the surface among all C-H bonds
z Cartesian coordinate normal to the surface of the injector

ε mean roughness of the nozzle wall
$\eta(x)$ Heaviside step function, $\eta(x) = 1$ for $x > 0$ and $\eta(x) = 0$ for $x < 0$
η_f viscosity of the fuel
κ heat conductivity
λ_b heat of vaporization
ν engine speed [rev/min]
ξ pair mixing fraction
ρ mass density
τ period for a full cycle, $2/\nu$
χ thermal diffusivity, κ/c
ω cycle-based angular velocity, $2\pi/\tau$

Abbreviations

BMEP	break mean effective pressure
CAD	crank angle degree
E10	gasoline with 10% ethanolic blend
HC	hydrocarbon
IMEP	indicated mean effective pressure
MFB50	CAD of 50% mass fuel burned
PRF95	95 w% isooctane, 5 w% heptane

indices of a quantity X

$\bar{X}$ time-averaged value and 0th Fourier coefficient of $X(t)$
X_0 value at the start of the accumulation of leaked fuel
X_a hydrogen abstraction by $RO_2\cdot$
X_{aOH} hydrogen abstraction by $RO\cdot$
X_b value at the point of boiling and precipitation

$X_{c,n}$	n^{th} even Fourier coefficient (multiplying cos $n\omega t$)
X^D	deposit phase
X^F	fuel film phase
X_i	initiation
X^M	metal phase
X_{NO}	branching by $\cdot NO + RO_2\cdot \rightarrow \cdot NO_2 + RO\cdot$
X_n	nozzle deposit
X_{OH}	formation of $RO\cdot$ by $2RO_2\cdot \rightarrow 2RO\cdot + O_2$
X_o	oxidation
X^S	surface
$X_{s,n}$	n^{th} odd Fourier coefficient (multiplying sin $n\omega t$)
X_t	termination
X_{tip}	tip deposit